Formation of Thermochemical Heterogeneities by Core-Mantle Interaction

Claudia Stein[1] and **Ulrich Hansen[1]**

[1]Institut f. Geophysik, Westfälische Wilhelms-Universität, Münster, Germany

Abstract Earth's core-mantle boundary (CMB) shows a complex structure with various seismic anomalies such as the large low shear-wave velocity provinces (LLSVPs) and ultra-low velocity zones (ULVZs). As these structures are possibly induced by chemically distinct material forming a layer above the CMB, models of mantle convection made ad hoc assumptions to simulate the dynamics of this layer. In particular, density and mass were prescribed. Both conditions are critical for the dynamics but hardly constrained. Core-mantle interaction is considered as one possible origin for this dense layer. For example, diffusion-controlled enrichment of iron has been proposed. We here apply a chemical gradient between the mantle and the denser core to analyze the penetration of dense material into the mantle. As such, we employ 2D Cartesian models where a thermochemical layer at the base of the mantle develops self-consistently by a diffusive chemical influx. Our simulations indicate that chemical diffusion is strongly affected by the convective mantle flow. This convection-assisted diffusion yields a compositional influx mainly in the areas where slabs spread over the bottom boundary and sweep dense material aside to form accumulations with rising plumes atop. Like for a prescribed dense layer this process leads to chemically distinct piles, which are typically smaller (therefore more suited to explain ULVZs) but more persistent due to the constant chemical influx. Combining the influx scenario with the primordial layer can possibly explain the simultaneous existence of LLSVPs and ULVZs along with the observation of a core-like isotopic composition in the mantle.

Plain Language Summary The core-mantle boundary (CMB) shows a complex structure. Seismologists have observed features that are possibly denser than their surroundings. These structures form from a dense layer above the CMB. Therefore typical mantle convection models have assumed an initial dense basal layer. The thickness and density of this prescribed layer are crucial but hardly constrained. Here we investigate core-mantle interaction as one possible origin for this layer and employ 2D Cartesian models of mantle convection that consider a diffusive chemical gradient between the iron-rich core and the silicate mantle. Our simulations show that the diffusive influx is coupled to the convective mantle flow. Convection-assisted diffusion gives a larger influx beneath slabs spreading over the CMB. Additionally, as in the models with a prescribed layer, the rising plumes pull dense material up and form piles. In this study, however, the constant chemical influx leads to piles existing for longer times. The piles are typically smaller but can maybe in combination with a primordial layer explain different seismologically observed structures and the presence of core material in the mantle.

1. Introduction

The deep Earth is of particular interest because on the one hand the presence of a large variety of thermal and chemical structures in the lowermost mantle has been reported (e.g., Garnero, 2000; Garnero & McNamara, 2008; Lay, 2015; McNamara, 2019) and on the other hand the core-mantle boundary (CMB) marks a special transition where solid silicate rocks of the mantle interact with the underlying iron-rich liquid of the outer core (cf. Dehant et al., 2022; Garnero et al., 2016; Lay et al., 1998; Rizo et al., 2019; and references therein).

The most prominent structures are the two large regions antipodally located beneath the central Pacific and Africa (e.g., Dziewonski, 1984; Grand et al., 1997; Romanowicz, 2001). These large low shear-velocity provinces (LLSVPs), occupying approximately up to 8% of the total mantle volume (Cottaar & Lekic, 2016), are characterized by their low seismic velocities (e.g., Hernlund & Houser, 2008; Wen, 2001). Additional smaller structures, the ultra-low velocity zones (ULVZs), have also been observed (e.g., Garnero et al., 1989). It has been proposed that both structures might be related as the ULVZs often occur at the edges of the LLSVPs (cf. McNamara, 2019).

The seismically observed (locally) sharp boundaries of the LLSVPs (Gleeson et al., 2021) and their stability in space and time has led to the thought that both structures might be of chemical nature (e.g., Forte & Mitrovica, 2001; Ishii & Tromp, 1999; Ni & Helmberger, 2003; Sun et al., 2009; Wicks et al., 2010) but this is still debated (Koelemeijer, 2020). For example, the larger reduction in S-wave velocity than in P-wave velocity for the ULVZs could also be an indication of partial melt (Rost et al., 2005). However, if the ULVZs are purely thermal structures, they should be located within the piles (where the hottest regions are) rather than at their edges, so that partial melt alone will also be insufficient (cf. Bull et al., 2009; McNamara, 2019).

Due to the various interpretations different modeling approaches have been considered, such as thermal plumes (e.g., Schubert et al., 2004; Stein et al., 2020) or thermochemical piles (e.g., Kellogg et al., 1999; McNamara & Zhong, 2005; Steinberger & Torsvik, 2012; Stein et al., 2020).

Thermochemical models have shown that a chemically heavier (dense) layer forms hot and dense piles under the influence of the convective flow in the mantle (e.g., Davaille, 1999; Gurnis, 1986; Hansen & Yuen, 1988; Jellinek & Manga, 2004; Langemeyer et al., 2020; Lassak et al., 2010; Steinberger & Torsvik, 2012; Trim & Lowman, 2016). The dense material is swept away from subducted regions and accumulates into piles below the rising plumes (e.g., McNamara & Zhong, 2005; Stein et al., 2020). Additionally, plumes at the edges of the piles were observed (e.g., Heyn et al., 2018; Mulyukova et al., 2015), which have been associated with volcanic hotspots typically found at the edges of LLSVPs (Garnero et al., 2016; Steinberger & Torsvik, 2012), and that may manifest themselves at the surface as eruption sites of large igneous provinces (LIPs) and kimberlites (Torsvik et al., 2006). McNamara et al. (2010) report that small, denser structures (ULVZs) usually reside at the edges of the large compositional reservoirs (LLSVPs) and as a portion of the dense material is entrained by the rising currents (e.g., McNamara et al., 2010; Tan & Gurnis, 2007), this might be an explanation for the different chemical reservoirs associated with the ocean island basalts (OIBs) and mid-ocean ridge basalts (Jellinek & Manga, 2004; Kellogg et al., 1999; Lay et al., 1998). For example, isotope signatures of core material in some OIBs may hint at the penetration of liquid iron from the core into the mantle explaining thus also the higher density of ULVZs (Rizo et al., 2019).

Regarding the origin of dense material in the deep mantle, there are various assumptions (e.g., Trønnes et al., 2019). Subducted and segregated oceanic crust that accumulates above the CMB (e.g., Brandenburg and van Keken, 2007; Frost & Rost, 2014; Jones et al., 2020; M. Li & McNamara, 2013; Mulyukova et al., 2015; Niu, 2018; Tackley, 2011) has been considered, but M. Li and McNamara (2013) suggested that the present-day subducted oceanic crust is not thick enough (i.e., it does not have enough negative buoyancy) and will rather be mixed into the ambient material than to form massive stable structures at the LLSVPs. M. Li et al. (2014) and Gleeson et al. (2021) argue that only ~10% of subducted crust can be stored in the LLSVPs and that rather more than one process is responsible for the formation of these structures. Further possible origins for a deep dense layer (see also review of Dehant et al. (2022) and references therein) are iron-rich accumulations from (a) a primordial layer of the early Earth, possibly as remnant of the crystallization after the magma ocean phase following the Moon-forming giant impact (Deschamps et al., 2012; Labrosse et al., 2007; Laneuville et al., 2018; Lee et al., 2010; Solomatov, 2015) or (b) the interaction between core and mantle material in which iron-rich core material enters the lower mantle (Buffett et al., 2000; Hayden & Watson, 2007; Knittle & Jeanloz, 1991; Mao et al., 2006; Otsuka & Karato, 2012; Petford et al., 2005).

The observed abundance of highly siderophile elements (HSE) in the Earth's mantle (i.e., elements that tend to form alloys with iron and are therefore mostly concentrated in the Earth's core) could be an indication for metal-silicate interaction at the CMB (Brandon et al., 1998; Walker & Walker, 2005). Additionally, a ^{182}W variability is seen as a strong evidence for core-mantle interaction (e.g., Mundl et al., 2017). The moderately siderophile element tungsten will have partioned into the Earth's core during metal-silicate segregation, Hafnium, however, is a strongly lithophile element and therefore concentrates in the silicate. After segregation the short-lived ^{182}Hf decays to ^{182}W explaining the enrichment of ^{182}W in Earth's modern mantle compared to chondritic meteorites (Rizo et al., 2019). The core will retain the tungsten isotopic composition at the time of formation, that is, a depletion in ^{182}W (Brandon & Walker, 2005; Kleine et al., 2009). As the tungsten concentration in the core is also assumed to be much larger than in the mantle, ^{182}W deficits (detectable in the ^{182}W/^{184}W ratio) in OIBs are considered as evidence for a chemical interaction at the CMB (Brandon & Walker, 2005; Rizo et al., 2019; and references therein).

Various experimental studies have also shown that core-mantle exchange can take place. For example, in the study of Hayden and Watson (2007) the grain-boundary diffusion of core elements through the polycrystalline MgO (periclase) of mantle rock is reported: the large atoms of core metals (that cannot diffusive through the mantle rock crystals) are able to move along the surfaces formed between adjacent grains of rock crystals. Furthermore, Hayden and Watson (2007) find that the diffusivities are high enough to transport siderophile elements tens of kilometers up into the mantle in a billion years. Likewise Mao et al. (2006) argue that diffusive processes at the CMB lead to the formation of iron-enriched post-perovskite that in the presence of mantle convection can rise higher into the mantle. Otsuka and Karato (2012) hypothesize that diffusion (maybe with the exception of grain-boundary diffusion for some elements) could be too slow. Further, they argue that infiltration either due to a pressure gradient where slabs cause topographic lows in the CMB (Kanda & Stevenson, 2006) or due to a capillary mechanism (Poirier & Le Mouël, 1992) will only explain iron penetration of 100 m or less into the mantle. Their experimental observations instead suggest that a morphological instability leads to iron-rich regions 50–100 km above the CMB. This instability is caused by the chemical potential gradient between the oxygen under-saturated core (which is predominantly composed of iron-rich metal) and (Mg, Fe)O crystals in the mantle.

Here we numerically address the possibility of a diffusive transport of dense material across the CMB. Employing a diffusive chemical influx at the bottom boundary of our model domain we are able to parametrize the entrainment of dense material into the mantle. We analyze how the material is entrained and if the mechanism is sufficient to explain large structures at the base of the mantle. Therefore we compare our results to models following the typical approach of an initially prescribed layer that represents a remnant of the magma ocean. In the latter models a no flux bottom boundary is employed that does not account for any core-mantle interaction. We discuss the evolutionary path of both systems and compare the modeled pile structures.

2. Model

The non-dimensional conservation equations for mass, composition, temperature and momentum for an incompressible Boussinesq fluid with infinite Prandtl number are given as:

$$\boldsymbol{\nabla} \cdot \boldsymbol{v} = 0, \tag{1}$$

$$\frac{\partial C}{\partial t} + \boldsymbol{v} \cdot \boldsymbol{\nabla} C - \frac{1}{Le} \boldsymbol{\nabla}^2 C = 0, \tag{2}$$

$$\frac{\partial T}{\partial t} + \boldsymbol{v} \cdot \boldsymbol{\nabla} T - \boldsymbol{\nabla}^2 T = H + H_c \cdot C, \tag{3}$$

$$-\boldsymbol{\nabla} p + \boldsymbol{\nabla} \cdot \boldsymbol{\sigma} + Ra(T - BC)\boldsymbol{e}_z = 0, \tag{4}$$

with the equation of state:

$$\rho = \rho_0[1 + \alpha \Delta T(BC - T)] \tag{5}$$

where $\boldsymbol{v} = (u, w)$ is the velocity vector, t is the time, p is the dynamic pressure, $\boldsymbol{\sigma}$ is the stress tensor, $\boldsymbol{e}_z$ is the unity vector in z-direction, ρ is the density (with ρ_0 defined at the surface), α is the thermal expansion coefficient, ΔT is the super-adiabatic temperature difference across the domain, and C and T are the chemical and thermal component, respectively. H is the nondimensional heating rate (cf. Stein et al., 2013) and H_c is a composition-dependent heating rate that only acts where the composition C is non-zero, that is, heating has its strongest effect within the piles (cf. Deschamps & Tackley, 2008; Kellogg et al., 1999; Y. Li et al., 2019). Both parameters are set to zero throughout most of the study and are only considered when analyzing the effect of flow parameters on the piles.

The thermal Rayleigh number, the buoyancy number and the Lewis number are defined as:

$$Ra = \frac{\alpha \rho_0 g \Delta T d^3}{\kappa_T \eta_0}, \quad B = \frac{\Delta \rho}{\alpha \rho_0 \Delta T}, \quad Le = \frac{\kappa_T}{\kappa_C}. $$

with the gravitational acceleration, g, the mantle thickness, d, and the density difference (at surface temperature) between the compositionally distinct material and its surrounding, $\Delta \rho$. κ_T and κ_C are the thermal and chemical

a) No flux cases (primordial layer scenario)
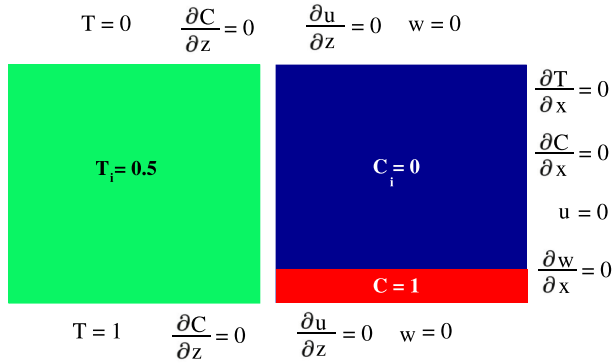
b) Influx cases (core−mantle interaction scenario)
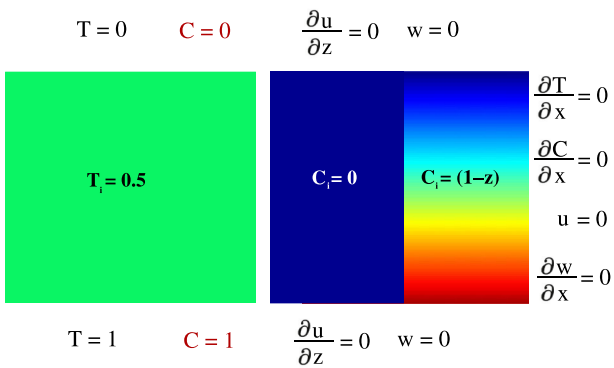

Figure 1. Boundary and initial conditions for (a) a system with an a-priori prescribed dense basal layer (i.e., no flux bottom boundary) and (b) for a system which applies a chemical influx from the core. In the influx case we either use a depleted mantle as initial chemical field ($C_i = 0$) or a stably stratified system with $C_i = (1-z)$ (right figure). The left figures show the initial temperature field ($T_i = 0.5$). In both scenarios reflective side conditions for the temperature and composition are assumed and free slip velocity boundary conditions with the velocity components u and w.

diffusivity and η_0 is the dynamic viscosity at the surface. As the Rayleigh number uses η_0, it is defined at the top boundary and increases with depth due to the temperature dependence of the viscosity. The buoyancy number describes the density contrast between the dense and the surrounding material. For reference values taken from Trim et al. (2014), that is, $\Delta T = 2500$ K, $\alpha = 1.2 \cdot 10^{-5}$ K^{-1}, and $\rho_0 = 3,300$ kg/m^3, a buoyancy number of $B = 1$ yields a density contrast $\Delta\rho$ of 99 kg/m^3 which corresponds to 3% of the reference density.

The dynamic viscosity is a function of temperature, composition, depth and stress (cf. Stein et al., 2004) in the form of:

$$\eta = \frac{2}{1/\eta_{pT} + 1/\eta_\sigma} \quad (6)$$

with a temperature-, depth- and composition-dependent part:

$$\eta_{pT} = \exp\left[-(\ln \Delta\eta_T)T + (\ln \Delta\eta_p)(1 - z) + (\ln \Delta\eta_C)C\right] \quad (7)$$

and a stress dependence:

$$\eta_\sigma = \eta^\star + \sigma_Y / \dot{E} \quad (8)$$

to allow for rigidly moving plates. Plate motion was shown to be necessary for the formation of piles, because a simple stagnant lid surface only causes a flat dense basal layer in response (Trim et al., 2014). Furthermore, we will show in this work, that the subducting slabs reaching the base of the system are important for a strong chemical influx from the core. In Equation 7, $\Delta\eta_T$, $\Delta\eta_C$, and $\Delta\eta_p$ are the viscosity contrasts due to temperature T, composition C and height z. In Equation 8, η^* is the plastic viscosity, σ_Y the yield stress and $\dot{E}$ the second invariant of the strain-rate tensor.

Dependencies such as a composition-dependent viscosity have been discussed in earlier studies (e.g., Stein et al., 2020) and have been considered in particular relevant for the stability of thermochemical structures (e.g., Heyn et al., 2018). Here, we focus on the mechanism of core-mantle interaction by a chemical influx and therefore mostly apply a rather simple rheological approach, but we additionally present some results of further dependencies to show their effect on the pile structure. Another parameter that has therefore been considered is a depth-dependent thermal expansivity:

$$\alpha(z) = \left(\frac{\alpha_0}{m(1 - z) + 1}\right)^3 \quad (9)$$

with α_0 the expansivity at the surface and m the factor of depth dependence (Stein et al., 2004).

We employ plaatjes which uses a finite-volume method for spatial discretization and the Crank-Nicolson method for temporal discretization. The equations are solved iteratively using the multigrid method with SIMPLER as smoother (Tosi et al., 2015).

2.1. Model Setup

Special attention has to be paid to the model setup. As first-order parametrization of a diffusive chemical influx at the base of the system, we use Dirichlet boundary conditions for the composition.

Figure 1 summarizes the initial and boundary conditions for our simulations as compared to the typically used model setup (Figure 1a). The latter simulations apply no flux composition conditions (Neumann condition: $\partial C/\partial z = 0$) as top and bottom boundary and the initial compositional field is given by a layer of dense material

($C = 1$) at the bottom of an otherwise depleted system ($C_i = 0$). The excess density and volume of this dense layer are arbitrarily chosen (e.g., Heyn et al., 2018; Langemeyer et al., 2020; Lassak et al., 2010; McNamara & Zhong, 2005; Stein et al., 2020; Trim & Lowman, 2016) and will be varied throughout this study. We refer to this kind of setting as the no flux cases (or primordial layer scenario).

Here, we propose a different setting (labeled influx cases) in which piles develop from a self-consistently formed dense layer. Figure 1b shows the changed top and bottom boundary for the composition field in red ($C = 0$ and $C = 1$, respectively). The isochemical bottom condition allows for an influx of compositionally dense material from below. In this way we do not have to prescribe an a-priori dense layer. Instead we consider two extreme initial conditions. In the one scenario the initial condition is a fully depleted system ($C_i = 0$). In a second scenario we consider a linear starting profile ($C_i = [1 - z]$) to approximate the stable compositional stratification after the magma ocean phase (e.g., Zaranek & Parmentier, 2004). In this way we can analyze the core-mantle interaction in a mantle that is already chemically enriched toward the CMB. In the Supporting Information we also present the result of an in-between scenario which has a thin dense basal layer (cf. Ballmer et al., 2017) but otherwise depleted mantle as initial condition (see Figure S1 in Supporting Information S1).

In all simulations the boundary conditions for the temperature are isothermal at the top and bottom and reflecting at the sides. All boundaries are free slip and impermeable. An initial temperature of $T_i = 0.5$ is applied. For comparison, an influx case in which the initial field is given by a hot interior ($T_i = 0.92$) is presented in Figure S1 in Supporting Information S1. We find the same evolutionary path as for the reference cases discussed here showing the robustness of the mechanism against initial conditions.

The input parameters of the reference model simulations are: a surface Rayleigh number of 10^4, a buoyancy number of $B = 1$, a Lewis number of $Le = 10$, viscosity contrasts due to temperature of $\Delta\eta_T = 10^5$ and composition of $\Delta\eta_C = 1$, and due to depth of $\Delta\eta_p = 1$. The effective viscosity is $\eta^* = 10^{-3}$ and the yield stress is $\sigma_Y = 4$. This gives a basal Rayleigh number of about 10^9. There is no variation in thermal expansivity with depth and no internal heating. It was shown that internal heating in Cartesian models lead to too high mean temperatures (because of the CMB being as large as the surface boundary) and can thus be neglected in order to better fit the mean temperatures of sherical shell models (O'Farrell & Lowman, 2010). Influx case 1 considers the initially depleted mantle and influx case 2 starts from the initially linear composition profile. For comparison, we present the results of two calculations considering the no flux condition with an initially prescribed dense basal layer (see no flux case 1 and no flux case 2 in Supporting Information). All the other parameters are the same as for the reference influx cases discussed here.

All simulations have been performed in a 2D box of aspect ratio 4 with a resolution of 512×256. Additionally, a grid refinement toward the upper and lower boundary has been applied to ensure that the fine structures at the lower boundary are resolved.

3. Results

3.1. Mechanism of Convection-Assisted Diffusion

The general behavior of influx case 1 (with an initially depleted compositional field) that allows for a chemical influx from the core is shown in Figure 2. The snapshots of the color-coded temperature and composition fields (Figures 2a and 2b, respectively) display the temporal evolution from top to bottom. In Figure 2c the corresponding depth profiles of the composition field are visible.

Time step $t = 0$ shows the initial temperature and the initially depleted composition field, which results in a depth-profile being zero over the whole depth with an increase only over the bottom boundary where chemical diffusion ($C = 1$) is given.

At $t = 0.0011$ we can see the first instabilities occurring in the temperature field. The subducting cold slab at the right boundary of the system sweeps the plumes at the base to the left. Consequently, the surface plate moves from the left to the right (Figure S2 in Supporting Information S1 displays the surface mobility for this simulation revealing steady plate motion over time). The composition field displays finer chemical instabilities at the exact same positions of the plumes. Like in typical pile simulations (cf. no flux case 1 in Supporting Information S1 (Figure S3)) we observe that dense material is entrained by the rising plumes. As such, a thin dense layer beneath sinking thermal currents and a thickened dense layer beneath rising thermal currents is observed which
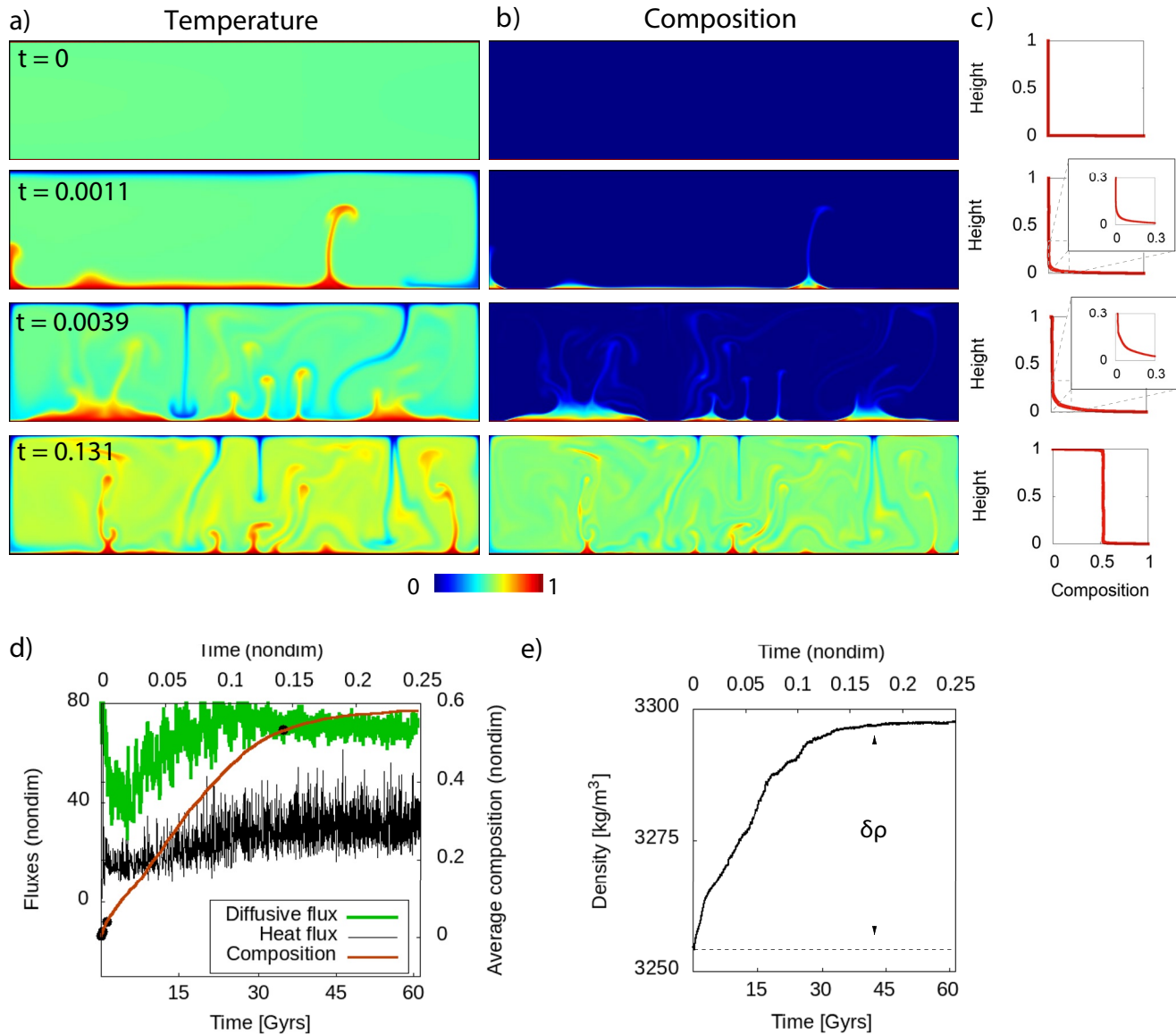
Figure 2. Influx case 1: (a) Snapshots of the temperature and (b) composition field for different time steps with (c) corresponding depth profiles of the composition. (d) Temporal evolution of the average heat flux (thermal Nusselt number), the average composition and the basal diffusive flux of the composition $\partial C/\partial z$ (=chemical Nusselt number times Lewis number). The dots mark the time points of the snapshots. (e) Temporal evolution of the average density computed from the equation of state showing the density increase $\delta\rho$ of about 48 kg/m³ over modeled time.

is similar to the observation in no flux simulations with a prescribed dense layer (e.g., Lassak et al., 2010; Stein et al., 2020). In this study, however, initially a depleted mantle was assumed and the dense material is naturally obtained by the diffusive influx at the CMB, which we will discuss in more detail in the following figures.

With time, more dense material is located in the mantle which leads to broader piles at $t = 0.0039$. The composition profiles show that dense material penetrating the mantle from the core rises upwards. For $t = 0.0039$ the profile displays that the composition in the deep mantle ($z < 0.2$) is increased compared to earlier time steps. Due to entrainment by plumes dense material is carried upwards in the following time steps, so that for the time $t = 0.131$ the profile shows a composition value of about 0.55 over the whole domain.

The average composition in the mantle (red line in Figure 2d) initially increases strongly with time, but only very slowly after $t = 0.131$ where $C > 0.5$. Consequently, as the composition in the system increases, the chemical gradient over the bottom boundary is affected. Here we plot the chemical Nusselt number times Lewis number,
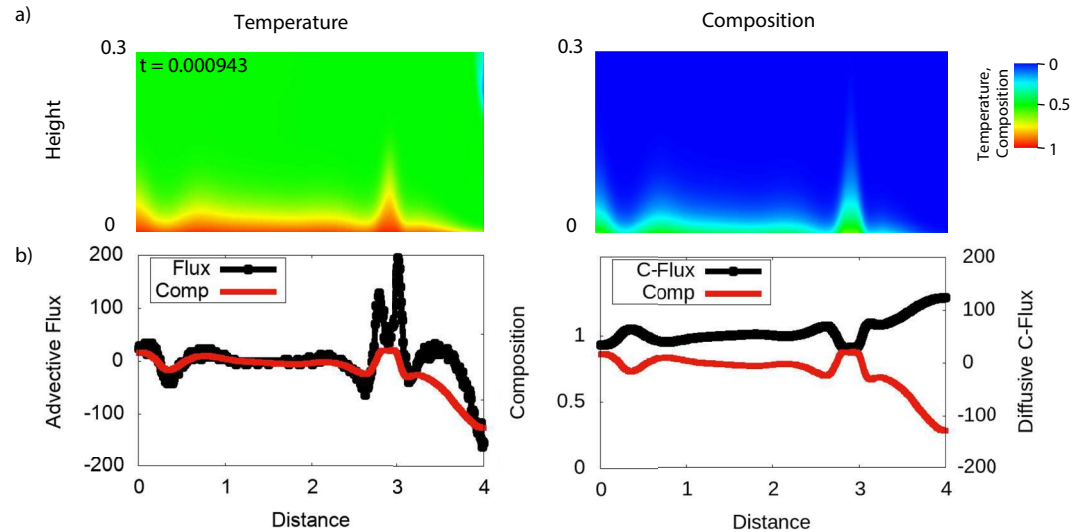
Figure 3. (a) Magnification of the lowermost 30% of the temperature (left) and composition field (right) at the non-dimensional time $t = 0.000943$ for influx case 1 (vertical axis is extended by a factor of 7). (b) Corresponding horizontal profiles of the composition (red lines), the total advective flux $wT + wC$ (left) and the compositional diffusive flux $\partial C/\partial z$ (right) at the base of the model domain.

that is, the diffusive influx is 10 times superelevated to plot it in the same range as the heat flux (Figure 2d). The chemical influx (green line in Figure 2d) is high at $t = 0$ (due to the depleted mantle) but strongly decreases as the average composition increases and a dense basal layer is formed. At $t \approx 0.02$ the influx again increases because at this point the convective flow becomes stronger. The average non-dimensional heat flux over time, also displayed in Figure 2d (black line), shows that the strength of convection increases until about $t = 0.131$ (~30 Gyrs). After this time the system is still strongly time-dependent but in a statistically stationary state. The strongly convecting system is characterized by thin plumes (cf. snapshots for $t = 0.131$). Additionally, at this time point we observe that the pile extent is considerably reduced. This agrees with the findings of McNamara and Zhong (2005) that the thermochemical structures are less wide for smaller density contrasts. As the background composition in our simulation has increased with time, the compositional contrast between piles and ambient material is reduced at later times. The increase in density can be seen in Figure 2e. Here we display the evolution of the volume-averaged density that has been computed from the equation of state (Equation 5) considering the temperature and composition fields. Like for the volume-averaged composition we find that the density first increases strongly with time until at approximately $t = 0.131$ where an almost constant value is reached. The change in average density over time due to the influx of core material is $\delta\rho = 48\frac{kg}{m^3}$, that is, a 1.45% density increase compared to the reference density. Note, that this is the value for the entire simulation, that is, when the steady state is reached. Considering the age of the Earth, we find that the change in density is only about $\delta\rho = 10\frac{kg}{m^3}$ (~0.3%). At this time point of about 4 Gyrs the chemical structures are still vast.

Overall, we observe the same behavior as in previous no flux cases (e.g., Lassak et al., 2010; cf. also the Supporting Information showing a simulation with the same parameters as influx case 1 but with a no flux condition) with the exception that here a dense layer at the base of the mantle forms self-consistently due to the basal chemical boundary condition ($C = 1$). As the layer formation is controlled by the chemical gradient over the CMB, not only the composition distribution but also the convective flow within the mantle plays an essential role. The subducting slabs sweep the dense layer aside causing a larger chemical gradient and the rising plumes entrain dense material forming dense accumulations that give a smaller chemical gradient. We analyze the impact of convective flow parameters further in the following section.

First we consider the basic mechanism. The temperature and composition field for an early time step of influx case 1 is shown in Figure 3. Here, the first instabilities start to form but the same behavior is observed throughout modeled time. At the right boundary of the model domain (distance $x = 4$) the thermal boundary layer (red area in left part of Figure 3a) is strongly thinned due to a cold downwelling at this position. A hot rising plume starts to form at approximately $x = 3$ and two smaller instabilities are visible at $x = 0$ and $x \approx 0.75$. In these locations

where the thermal boundary layer is thicker also a thicker chemical boundary layer (green area in the right part of Figure 3a) is observed. Likewise the dense layer is thinned where the sinking slab spreads over the boundary layer (at $x = 4$). As such, the horizontal profiles in the left part of Figure 3b also show the clear correlation of the total advective flux ($F_a = wT + wC$) and the composition C. The composition is high in the location of an upwelling flow represented by a positive advective flux (e.g., $x = 0$ and $x = 3$) and the composition is low at the position of a strong downflow with a negative advective flux ($x = 4$). As in earlier studies with the no flux condition (e.g., Steinberger & Torsvik, 2012), we thus observe that the dense material is entrained by the convective flow and pulled up to form piles whereas the dense layer is strongly thinned beneath subducting slabs.

The right part of Figure 3b again displays the composition (red line), but now along with the diffusive chemical influx (black line). The diffusive chemical flux dC/dz is computed at the base of the system and thus represents the in- and outflux over the CMB. A clear anticorrelation is observed, which is a natural consequence of the fixed composition of $C = 1$ at the bottom boundary (this is analogous to the relation between the heat flux and the temperature, cf. Langemeyer et al., 2022). The locations characterized by a high value of the composition field at the base of the mantle reveal a low chemical gradient (e.g., $x = 3$) while the locations with a low value of the composition field at the base of the mantle show a high gradient (e.g., $x = 0.5$ and $x = 4$). In this way, the chemical influx is also strongly coupled to the convective flow. As the dense material accumulates below upwellings, the high composition here diminishes the chemical influx but at places of a strong downwelling the chemical influx is high. The same result is observed at later times in the system, but with the stronger convection in the mantle the chemical influx is higher than for the early stage (cf. Figure 2d).

The effect of fluid dynamical parameters on the chemical influx is investigated more closely in the next section.

3.2. Parameter Study on the Chemical Influx and the Pile Structure

In a first step we analyze the mechanism of core-mantle interaction for varying Lewis, Rayleigh and buoyancy numbers. Here we relate the bottom chemical Nusselt number ($= \frac{1}{Le} \frac{\partial C}{\partial z}$, i.e., the diffusive influx scaled with the compositional diffusivity) with the RMS-velocity (which like the heat flux in Figure 2d is a measure for the strength of convection).

Obviously the Lewis number Le has a profound impact on the system as the compositional diffusivity determines the influx. Compared to the thermal diffusivity the chemical diffusivity is considered to be very low for iron-rich core material (e.g., Bouffard et al., 2019; Otsuka & Karato, 2012) and even lower in the mantle (Hansen & Yuen, 1988). In Figures 4a and 4b we therefore investigate an increasing Lewis number (i.e., decreasing chemical diffusivity). While there is no change in the steady state RMS-velocity, the Nusselt number strongly decreases due to the inverse of the Lewis number as prefactor.

In Figures 4c and 4d we present the behavior of influx cases with varying Rayleigh numbers. Increasing the Rayleigh number leads to a stronger diffusive influx at the base of the system (Figure 4c). This stronger diffusive influx correlates with the increase in the strength of convection (Figure 4d). Likewise we find that a reduction in buoyancy number gives an increase in the chemical influx (Figure 4e) and the strength of convection (Figure 4f). The snapshots of the composition field in Figures 4g and 4h show vast chemical structures for low Rayleigh numbers which hinder the influx over a wide range of the CMB (by reducing the chemical gradient in these areas) plus an insufficient entrainment of dense material to greater heights, while the high Rayleigh number case shows finer structures. Additionally, for a high Rayleigh number the strong convection carries more dense material high into the mantle. The thinner structures therefore also give off more dense material allowing for a higher influx at the CMB. We thus find that convection promotes the influx and refer to this process as advection- or convection-assisted diffusion.

A similar behavior was observed for influx case 1 with time (cf. Figure 2). As dense material is entrained high into the mantle, the density contrast between the piles and the ambient mantle and thus the buoyancy number (restoring force) is reduced. Therefore the convective strength increases with time and we obtain a higher compositional influx (Figure 2d). We have also seen the thinning of the rising plumes (Figure 2a), which consequently affects the pile structure (Figure 2b).

In Figure 5a we plot the distribution of the piles for influx case 1 at time $t = 0.0011$ together with that at $t = 0.131$. Here, we can clearly see that the piles at later times are smaller and thinner. We therefore further analyzed

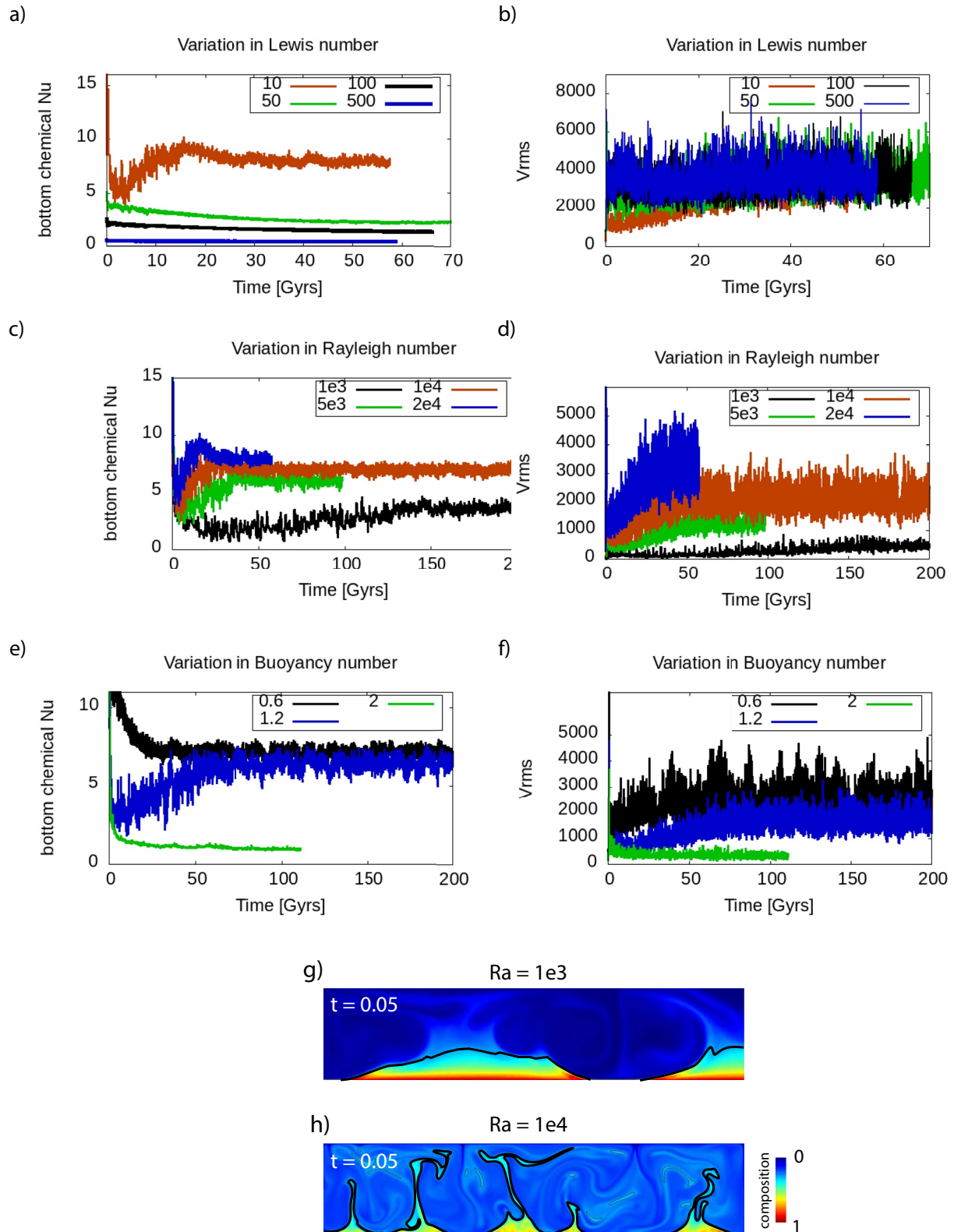**Figure 4.** Influx case 1: Temporal evolution of the chemical Nusselt number at the base of the system (left) and RMS-velocity in the complete system (right) for (a, b) different Lewis numbers (Ra = 10⁴, $B = 1$), (c, d) different Rayleigh numbers ($B = 1$, Le = 10), and (e, f) different buoyancy numbers (Ra = 10⁴, Le = 10). (g, h) Snapshots of the composition field for two Rayleigh numbers (black isoline: $C = 0.15$).
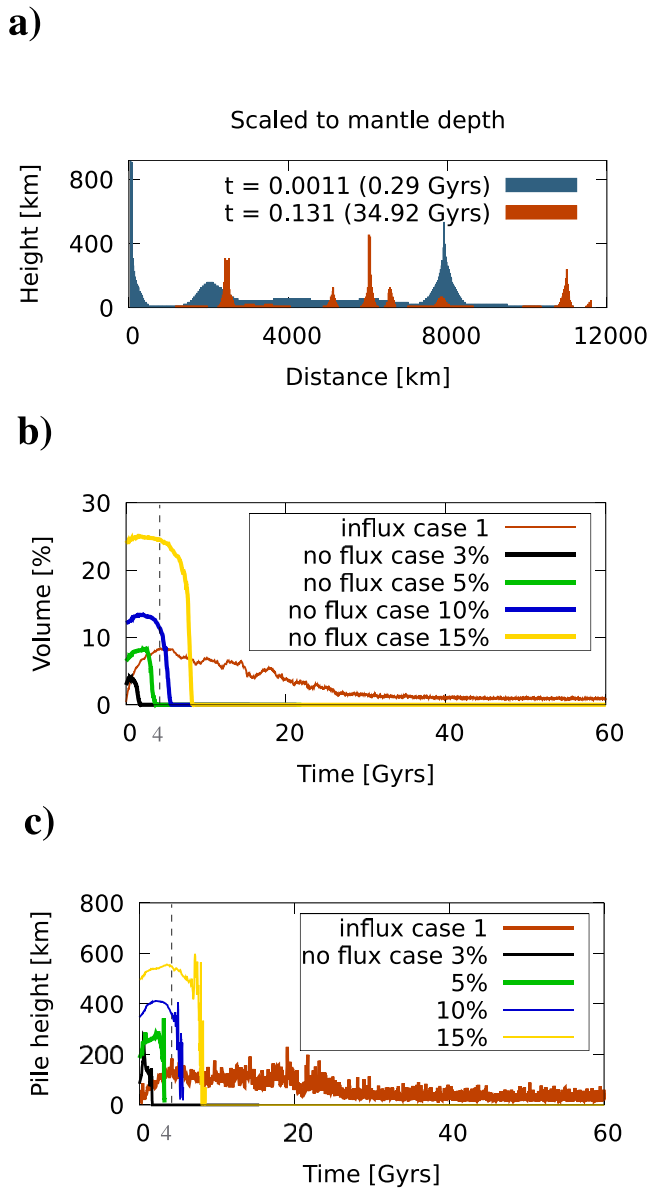
a)

b)

c)

Figure 5. (a) Influx case 1: pile distribution for two time points. (b) and (c) Temporal evolution of the pile volume and average height for influx case 1 and no flux cases as a comparison. In the no flux cases the volume of the initial dense layer is varied from 3% (no flux case 1) to 15% (no flux case 2). The pile height is spatially averaged for each time, so that the local peaks in panel (a) are not represented in Figure (c).

the temporal evolution of the pile volume and height for influx case 1 and compare it to cases with the same parameters but no flux composition boundary conditions (Figures 5b and 5c). A pile volume of 5% means that 5% of the model domain is covered by dense material (where dense material having a composition value $C \geq 15\%$ of the average composition is counted as pile). The pile height represents the spatially averaged height for each time step, thus single thin and high piles as seen in Figure 4h are not reflected.

We find that the evolution of the pile volume and pile height largely show the same picture. In every case the values first increase until they reach a maximum (this is when the dense layer is deformed and piles up). However, we observe that the model simulation with an influx of dense material (influx case 1) gives piles that exist over a longer time period (Figures 5b and 5c). For no flux boundary conditions the piles vanish as the dense material from the initially prescribed layer is entrained but there is no further influx of dense material. A larger volume of the initially prescribed layer in the no flux cases extends the time before the piles vanish but still falls below the time limit where the influx cases reach a steady pile volume. For example, for an initial layer that covers 15% of the modeled mantle volume the no flux case (no flux case 2) has piles for the period of ∼8 Gyrs while the influx case 1 at this time has piles that still cover ∼7% of the mantle volume and also has piles for more than 60 Gyrs. Within the life time of the Earth ($t < 5$ Gyrs) all simulations have reached their maximum pile size. The piles in the no flux cases have a time-averaged height of 150–550 km for the cases with the 3% to the 15% initial dense volume, respectively (Figure 5c). However, only the cases with a 10% and 15% volume still have piles at 4 Gyrs. Increasing the Lewis number also extends the survival time of the piles, so that also the initially thin layer case shows piles over the life time of the Earth, however, at the same time reducing the pile height considerably (cf. Figures S4e and S5e in Supporting Information S1). For the influx case the maximum volume of the piles is up to 8% and the average height up to 150 km. For this parameter set (i.e., Rayleigh number of 10^4 and Le = 10) we find that the values roughly match those of the no flux scenario with the 3%–5% initial primordial layer.

As seen before, the convective mantle flow also plays an essential role for the pile distribution. On the one hand we observed that piles accumulate beneath plumes, and as thermal structures become thinner with increasing strength of convection this affects the pile volume. On the other hand we observed that stronger convection promotes the chemical diffusion and also the entrainment of dense material to higher depths. We therefore investigated the simulations with varying fluid dynamical parameters with respect to the modeled pile behavior (Figure 6). The results are very similar to those of the no flux scenarios with an initial dense layer (cf. Figures S4 and S5 in Supporting Information S1).

An increase in the Lewis number dramatically decreases the piles' size, that is, pile volume and height (Figure 6a). The low chemical diffusivity only allows for a small basal chemical influx and also for little entrainment of dense material upwards. For the pile volume we observe that all simulations converge to a value of ∼1% and for the pile height to roughly 20 km. However, we again observe that the convective flow also strongly affects the piles' size. A low Rayleigh number (Figure 6b) and/or a high buoyancy number (Figure 6c) yield a rise in pile volume and height as in both cases the strength of convection is reduced, which leads to broader plumes and following from this to larger piles. For example, for the Rayleigh number of Ra = 10^3 the maximum pile volume is almost 20% and the maximum pile height about 700 km. For this Rayleigh number the values exceed those of the pimordial layer case with a 3% volume (maximum pile volume of ∼6% and height of ∼500 km) but more match those of the initial 15% volume (maximum pile volume of about 25% and height of 900 km; Figures S4 and S5 in Supporting Information S1).
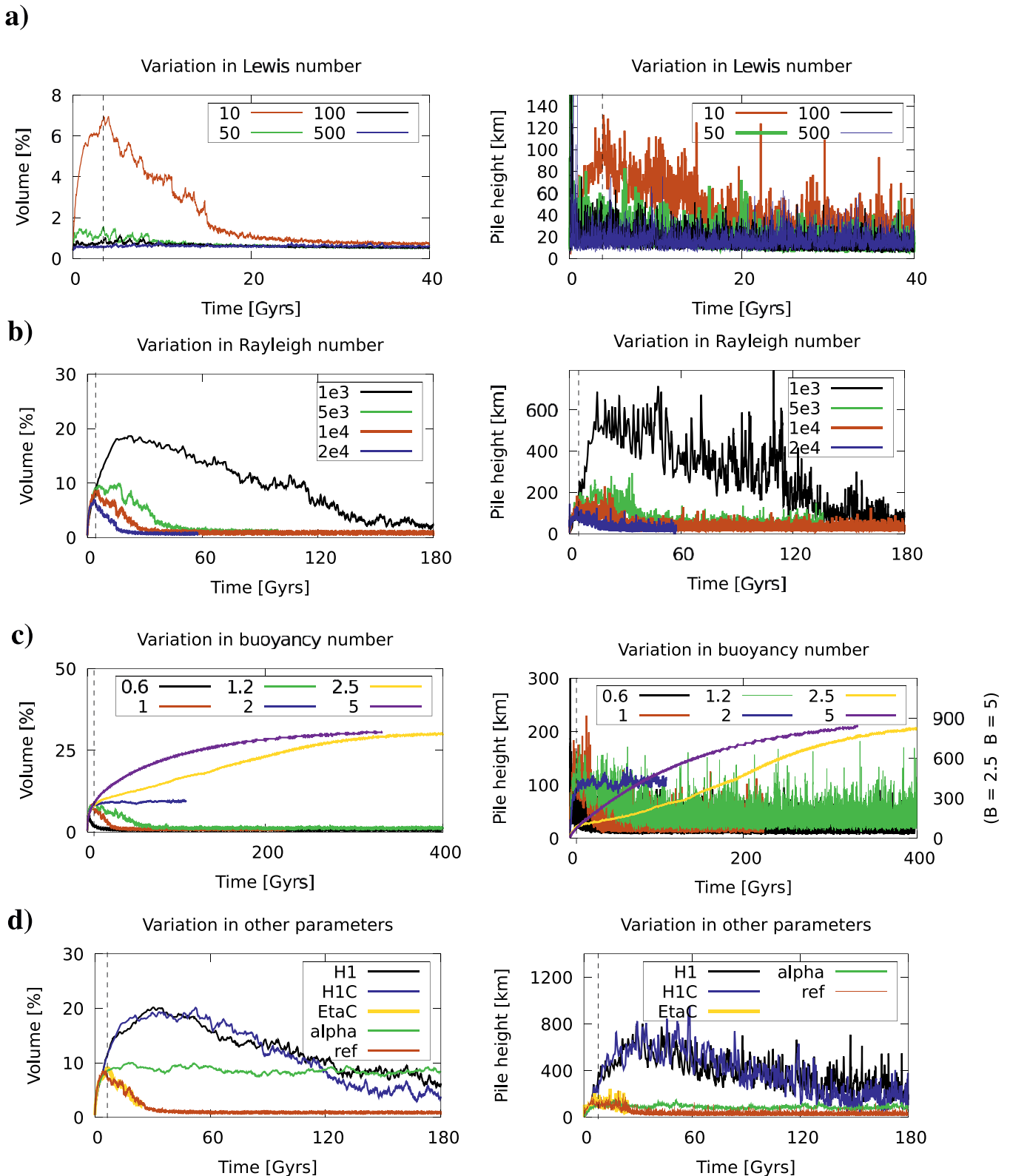
Figure 6. Influx case 1: Temporal evolution of the pile structure for different (a) Lewis numbers (Ra = 10^4, $B = 1$), (b) Rayleigh numbers ($B = 1$, Le = 10), (c) buoyancy numbers (Ra = 10^4, Le = 10), and (d) other parameters (Ra = 10^4, $B = 1$, Le = 10). For further parameters see reference case (influx case 1). Here H1 stands for a heating mode of $H = 1$, H1C for a composition-dependent heating of $H_C = 1$, EtaC for a composition-dependent viscosity with a viscosity contrast of $\Delta\eta_C = 10^2$, alpha for a model calculation with a thermal expansion coefficient that increases by a factor of 2 with depth, and ref for the reference case shown in Figure 2. The left figures show the pile volume and the right figures the average pile height at each time step. The dashed vertical lines highlight the time of 4 Gyrs.

We find that piles cover almost the complete bottom layer for a mildly convecting system (cf. also Figure 4g). Additionally, entrainment is strongly reduced so that over modeled time we do not observe a decrease in pile volume or height for the high buoyancy numbers (here for $B = 2$ and 5, i.e., density contrasts of 6% or larger). It seems that the pile volume remains constant or only diminishes very slowly. This is consistent with the findings of Mulyukova et al. (2015) who show that the growth rates of piles appear to be constant for large buoyancy ratios, while the growth rate seems to decline with time for low buoyancy numbers. In our $B = 0.6$ case we find that during the life time of the Earth, the pile size has already declined considerably, while the higher buoyancy ratio simulations show a constant or even increasing pile size (Figure 6c). This is also in agreement with, for example, Olson and Kincaid (1991) and Huang and Davies (2006), who find that high buoyancy ratios promote the survival time of dense accumulations. McNamara and Zhong (2005), Y. Li et al. (2014b), and Trim et al. (2020) also observe that thermochemical structures are wider and flatter for high buoyancy numbers. Increasing the buoyancy number (or likewise reducing the Rayleigh number) further would finally result in a conductive layer covering the entire bottom boundary. Entrainment then only occurs by diffusion which is much slower than by convection. Consequently, the density of this layer remains high for a long time and only decreases slowly, so that the influx of more core material is strongly reduced.

Finally, in Figure 6d we also present some simulations in which we varied additional pile-controlling parameters. A viscosity that depends on the chemical component (here a viscosity contrast of $\Delta\eta_C = 10^2$, yellow line) does not give a largely different picture than the reference case (red line). This seems different in the primordial layer scenario (Figures S4f and S5f in Supporting Information S1) but can be explained by the amount of dense material present. As we have seen before, the pile size in the reference case of the influx scenario is rather small, thus there is less material on which the composition-dependent viscosity can act. However, a depth-dependent thermal expansivity ($m = 0.3$ which leads to a decrease with depth by a factor of 2, green line) seems to have a stronger stabilizing effect on the piles. The pile volume is temporally stable and also increased compared to the reference case. Likewise the pile height is increased from 30 km in the reference case to 90 km for the simulation with a depth-dependent expansion coefficient α. The general behavior for these two simulations is understandable when comparing them to our other results. Increasing viscosity with depth by a composition dependence as well as reducing the thermal expansion coefficient with depth both lead to a reduction in the lower Rayleigh number. The results are therefore similar to reducing the Rayleigh number or increasing the buoyancy number. The composition-dependent viscosity, however, only has an effect where the composition field is high and is thus limited to a smaller area. Therefore the effect is smaller than for the thermal expansivity. An even larger effect is observed for the simulations which allow for internal heating. Both simulations show an increase in the pile volume and height. The average pile height, for example, in the steady state is ~170 km for the model calculation in which a compositionally dependent heating was assumed ($H_C = 1$, blue line) and slightly higher (~250 km) for the case with an overall heating of $H = 1$ (black line). This is probably due to a decrease in the temperature jump ΔT in the lower part of the model geometry as the interior temperature is increased. This again reduces the bottom Rayleigh number. The impact of the heating modes in the primordial layer scenario cases is less than for the influx case, which might be due to the convection-assisted diffusion. As we have seen before an increase in Rayleigh number more strongly affects the piles' size in the influx scenario than in the primordial layer scenario. The effect of these parameters, however, has to be investigated more closely in a further study, in particular their influence on pile structure and stability. Here, we concentrate on the mechanism of core-mantle interaction where these single simulations have shown that the mechanism is still valid.

Core-mantle interaction is therefore a viable mechanism that might account for the presence of some core material in the mantle that could also reach the surface at ocean islands. The existence of the large seismically observed structures might, though, be difficult to explain solely by this process if realistic parameters are employed. Therefore we also present the combination of two relevant scenarios as a possible explanation for the observations on Earth.

3.3. Combination of the Primordial Layer and Core-Mantle Interaction

Here we present a case in which the lower mantle is already enriched due to remnants of the magma ocean phase (e.g., Ballmer et al., 2017). In Figure 7 we show a model calculation (influx case 2) which has an initially linear composition stratification but otherwise the same configuration as influx case 1. The overall model behavior for both cases is very similar. At the location of the plumes, dense material is accumulating ($t = 0.00228$). The
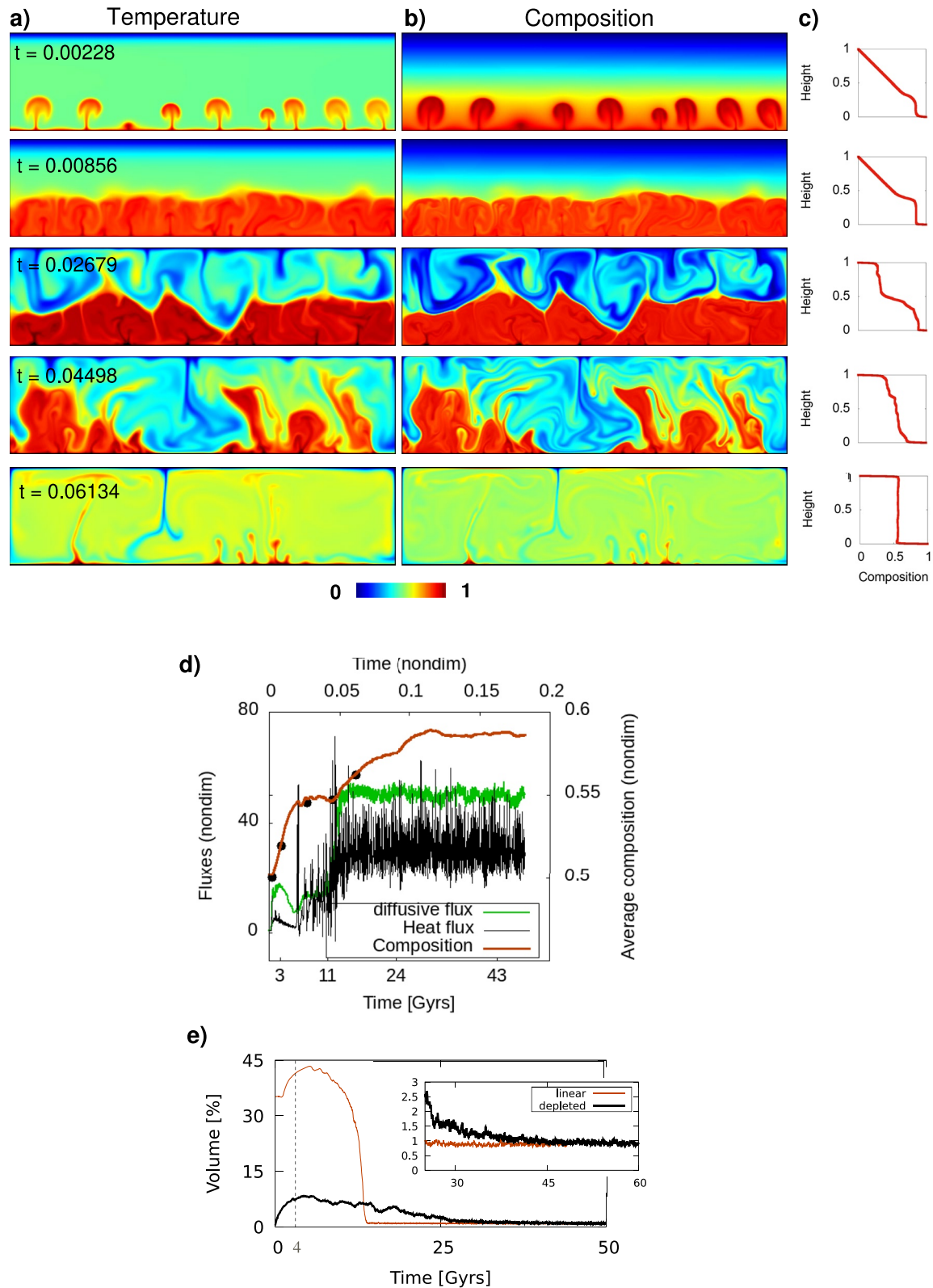
Figure 7. Model simulation with an initially stratified compositional field and an additional compositional influx at the bottom boundary (influx case 2). (a) Temperature and (b) composition fields at different times and (c) corresponding depth-profiles of the composition. Temporal evolution of (d) the heat flux (thermal Nusselt number), composition and diffusive influx, and of (e) the pile volume for influx case 2 with the linear starting condition in the composition (red line) compared to the pile volume for influx case 1 with a depleted mantle (black line).

composition-depth profile shows a first deviation from the initial linear stratification (at heights $z < 0.25$). As the hot plumes are now denser than the plumes in influx case 1, they do not rise as high and the dense material widely accumulates in the lower half of the model domain. An internal thermochemical boundary layer is formed (at $t = 0.00856$). The depth profile of the composition shows a clear step at the height of about 0.4. This layering behavior is also known from models with a no flux condition at the bottom boundary but a thick prescribed dense basal layer (cf. Figure S6 in Supporting Information S1). Small-scale instabilities form at this interior boundary and just as infiltration of dense material by the diffusive influx occurs at the bottom of the model domain, it is also present at the interior boundary. Therefore dense material is also slowly transported into the upper half of the box. The instabilities become stronger and at $t = 0.02679$ the layering breaks up leaving large-scale thermo-chemical structures ($t = 0.04498$) before thermochemical mixing finally leads to a homogeneous temperature and composition distribution (with an average composition of $C \approx 0.5$) with small plumes and piles ($t = 0.06134$). This final stage resembles that obtained in influx case 1.

Due to the higher initial composition in influx case 2 (note that the average composition in Figure 7d starts at $C = 0.5$), the averaged non-dimensional heat flux (black line) and chemical influx (green line) in Figure 7d initially reveal low values. As the lower layer starts to break-up (between the time panels of $t \approx 0.02$ and 0.05) the fluxes increase and finally reach a statistically steady state, revealing a vigorously convecting system. Again the mechanism of convection-assisted diffusion becomes visible by the diffusive influx following the same trend as the heat flux. The averaged composition (red line) shows an increase at the beginning, like seen for influx case 1, but during the time of layer break-up ($t \approx 0.02$ and 0.05) the composition remains almost constant at $C \approx 0.55$ until a further composition increase is observed after the break-up. At the non-dimensional time of $t \approx 0.12$ an almost steady composition of $C \approx 0.58$ is reached. This value is the same as in influx case 1 which, however, was reached later as the system of influx case 1 was initially depleted. The increase in density over the whole model time for this case is lower than for influx case 1 (here $\delta\rho \approx 10\frac{kg}{m^3}$; ~0.3% of the reference mantle density) due to dense primordial material being present in the mantle, which gives an increased initial density.

In Figure 7e we display the temporal evolution of the pile volume (red line) and compare this to influx case 1 that initially considered a depleted mantle (black line). In influx case 2, which has the linear composition stratification as initial condition, more dense material is present and as such the pile volume reaches higher values (volume >40% of the mantle). This is when we observe the layering. During the break-up phase ($t \approx 10$–15 Gyrs) the pile volume decreases considerably, which is also clearly visible when comparing the composition snapshots at $t = 0.04498$ and $t = 0.06134$. In the final state both influx cases yield almost the same pile volume of approximately 1%.

Considering the age of the Earth, this parameter set would place the Earth in the layering phase. However, the initial linear profile will rather be an extreme case. Ballmer et al. (2017) suggest a more exponential function. Combining the influx scenario with a thinner primordial layer on the one hand reduces the layer thickness and on the other hand does not give such an extensive layering phase (Figure S1 in Supporting Information S1).

4. Discussion

OIBs, which are regarded as the surface expression of deep mantle plumes, are geochemically distinct from samples of Archean terranes (e.g., Rizo et al., 2019). These deeply rooted plumes might have their origin in chemical structures in the D″ region, where variations in seismic velocities are observed and which are often attributed to the accumulation of dense material, possibly the enrichment of iron arising from core-mantle inter-actions (e.g., Mao et al., 2006; Otsuka & Karato, 2012; Petford et al., 2005). Besides core-mantle interaction, material stemming from recycled crustal components (e.g., Brandon & Walker, 2005; Rizo et al., 2019) or a dense primordial layer resulting from early metal-silicate fractionation during the magma ocean phase after the Moon-forming giant impact (e.g., Deschamps et al., 2012; Labrosse et al., 2007; Laneuville et al., 2018; Lee et al., 2010; Solomatov, 2015) have been considered to explain the geochemical structures of large low seimic velocity provinces (LLSVPs) and ULVZs at the CMB. In previous mantle convection studies an initially dense basal layer was prescribed (e.g., Davaille, 1999; Gurnis, 1986; Hansen & Yuen, 1988; Heyn et al., 2018; Jellinek & Manga, 2004; Langemeyer et al., 2020; Lassak et al., 2007, 2010; Steinberger & Torsvik, 2012; Trim & Lowman, 2016), but the excess density and volume of this layer are uncertain.

In order to explain the observed tungsten (^{182}W) deficits in OIBs, that is, an isotopic composition similar to that of the core, (e.g., Rizo et al., 2019) and the abundance of HSE in the Earth's mantle a number of core-mantle

interaction processes have been proposed from laboratory experiments (Hayden & Watson, 2007; Kanda & Stevenson, 2006; Otsuka & Karato, 2012; Poirier & Le Mouël, 1992). Some of them have, however, been considered to be insufficient because the diffusive mechanism is too slow and would only lead to iron penetration of only a few km into the mantle (Otsuka & Karato, 2012).

We numerically analyzed the possibility of infiltration of iron-rich material by chemical diffusion and compare the resulting structures to those that originate from the primordial layer scenario. Therefore we employed a thermochemical mantle convection model.

As calculations in a spherical geometry are computationally very demanding we limited our study to a 2D Cartesian geometry. In this way we were able to perform an extensive parameter study in order to analyze the system behavior. Furthermore, we used a wide box with an aspect ratio of 4 to minimize boundary effects. Earlier studies have shown that a change from the Cartesian geometry with reflecting boundaries to a cylindrical geometry with periodic boundaries results in the same system behavior with only an increase in plate mobility (e.g., Zhong and Gurnis, 1997). Consequently, we assume that our results will not be altered when transferred to a spherical geometry apart from maybe a reduction in spatial pile stability.

For simplicity we have also neglected the impact of phase transitions within the mantle. In particular, the transformation from bridgmanite to post-perovskite (ppv) a few hundred kilometers above the CMB (e.g., Kuwayama et al., 2022) can explain some seismic observations, such as the D″-discontinuity (e.g., Murakami et al., 2004; Oganov & Ono, 2004) or ULVZs (Mao et al., 2006). Y. Li et al. (2014a) and Nakagawa and Tackley (2011) analyzed the effect of low-viscosity ppv and observe that cold slabs spread more vastly above the CMB and more dense material is entrained in upwellings, which we have shown both promotes the infiltration of dense core material. Mao et al. (2006) consider diffusive processes at the CMB of importance for the formation of iron-rich post-perovskite and show that a ppv silicate phase, that contains up to 40 mol% $FeSiO_3$, leads to seismic wave velocities as observed in ULVZs. However, while Mao et al. (2006) consider ULVZs being made up by solid iron-rich ppv, the possibility of ULVZs being partially molten was also discussed (e.g., Trønnes et al., 2019). In their review, Trønnes et al. (2019) assume that ULVZs consist of only a low degree of iron-rich metallic liquids (largely derived by subducted oceanic crust) in a perovskite-dominated matrix (largely bridgmanite $MgSiO_3$ and some Ca-perovskite $CaSiO_3$), so that further studies could take a two-phase flow into account. Nonetheless, they conclude that at present (after the basal magma ocean has solidified) a reduced core-mantle exchange could occur via the partially molten ULVZs.

Here, we investigated diffusion-controlled infiltration of dense solid material by considering a diffusive chemical influx at the lower model boundary of a thermochemical mantle convection model. Typical models of the primordial layer scenario consider the tracer approach (e.g., Langemeyer et al., 2022; Lassak et al., 2010), but we have shown that the same behavior is obtained in the field approach (Stein et al., 2020 and Supporting Information). We therefore employed a Dirichlet condition as bottom boundary condition (Figure 1) using the field approach, which allows for the investigation of a varying Lewis number. In this way estimations of more realistic values can be made. As the Lewis number describes the chemical diffusion its value is critical for this influx scenario. While a Lewis number of infinity is applied in the tracer approach, in the case of the field approach a numerical reasonable Lewis number is below the realistic value. For example, the Lewis number is considered to be maybe even as large as 10^{13} in the Earth's mantle (Kellogg & Turcotte, 1987). Here, we assume that core material infiltrates the mantle. Therefore, in the influx scenario we follow assumptions of Hayden and Watson (2007), Otsuka and Karato (2012), Bouffard et al. (2019), and Meyer et al. (2019) where the chemical diffusivity could be in the range of $10^{-9} \frac{m^2}{s}$ (amounting to a Lewis number of only 10^3) for iron or HSE.

The comparison of the results from the influx scenario to those of the primordial layer scenario (with no basal influx) shows that both scenarios give a qualitatively similar behavior. In the primordial layer scenario we have a prescribed dense layer while it is self-consistently growing in the core-mantle interaction scenario. Subducting slabs push the (growing or prescribed) dense layer to the side and the dense material accumulates beneath the hot rising currents forming dense piles (e.g., McNamara & Zhong, 2005; McNamara et al., 2010; Steinberger & Torsvik, 2012; Stein et al., 2020). Where the slabs reach the CMB the thermochemical boundary layer is thinner (Figure 2) and in the influx scenario this leads to a stronger chemical gradient over the boundary than beneath dense piles (Figure 3). Thus the infiltration of dense core material largely occurs at the position of slabs. This is similar to the infiltration by suction due to a pressure gradient at CMB depressions described by Kanda and Stevenson (2006).

The amount of material accumulating depends on the compositional gradient between the mantle and the core and as such we observe that the convection in the mantle has a profound impact. Not only is the largest influx observed at the subduction zones but also the fluid dynamical parameters play an essential role (Figure 4). We identify the process of convection-assisted diffusion.

The primordial dense layer scenario (with the no flux condition) and the forming dense layer scenario (due to the chemical influx) only differ in the size and longevity of the modeled piles. Due to the low compositional influx the growing layer is rather thin, thus giving only relatively small piles. However, the piles in the growing layer scenario increase more strongly with increasing strength of convection than the piles in the primordial layer scenario. We find that the pile size in the influx scenario with an Earth-like Rayleigh number of 10^8 resembles that of the primordial layer scenario with an initial dense layer of 3%–5% of the modeled mantle volume. The size of the piles in the primordial layer scenario also strongly depends on the initial thickness of the dense basal layer. To match the LLSVPs on Earth, which are assumed to have a height of about 100s of kilometers (McNamara, 2019) and a volume of 8% of the Earth's mantle volume (Cottaar & Lekic, 2016), our results suggest that an initial dense layer of about 10% of the Earth's mantle volume seems reasonable. For example, for our reference case with a Rayleigh number in the realistic range of about 10^8 in the mid-mantle and a density contrast of 3%, the modeled piles reach a maximum height of about 270 km (and pile volume of ∼4%) for an initial layer thickness of 3% and 570 km (volume of ∼25%) for a 15% volume layer. The scenario of core-mantle interaction leads to a maximum pile height of 230 km (pile volume of ∼9%) (Figure 5). The smaller pile height in the influx scenario thus suggests that these modeled piles are more suited to explain the smaller ULVZs rather than the two large LLSVPs observed in the Earth. The latter are better explained by the primordial layer scenario.

As mentioned above, due to the convection-assisted diffusion the choice of parameters has a huge impact on the modeled piles. While the Rayleigh number in our given example is in a realistic range for the Earth's mantle, the Lewis number is too low. This low value promotes the chemical diffusion more strongly than is realistic. In a systematic parameter study on the effect of the Lewis number, we find that the pile height decreases from about 270 km (Le = 10) to 100 km (Le = ∞) (pile volume from 4% to 3.5%) in the primordial layer scenario with a 3% layer volume (Figure S5 in Supporting Information S1) and from 230 km (Le = 10) to 80 km (Le = 500) (pile volume from 7% to 0.9%) in the influx scenario (Figure 6). The decrease in pile volume is even stronger for the influx case than for the primordial layer case, because for the primordial layer scenario the lower chemical diffusion (higher Lewis number) only diminishes the entrainment of dense material by plumes. The piles thus erode more slowly when increasing the Lewis number. The same holds for the influx scenario but here the low chemical diffusivity (high Lewis number) also considerably reduces the influx. Extrapolating our influx results to more realistic Lewis numbers of the order of 10^3 or 10^4 (penetration of iron from the core) suggests a modeled pile height of roughly 10 km which is at the lower end of the assumed pile height of ULVZs and supports the thought that diffusion is a too weak process to explain the ULVZs (Otsuka & Karato, 2012).

However, in this work we showed that the diffusion process is strongly assisted by convection. In a vigorously convecting mantle the accumulation of dense material by diffusion is much faster and entrainment is more efficient. Consequently, the modeled piles are relatively small. In weakly convecting systems the penetration and entrainment of dense material is slower so that vast pile structures form (e.g., Figures 4g and 4h). For example, we find that increasing the buoyancy number also decreases the chemical influx (Figure 4e) as the strength of convection decreases (Figure 4f). Varying the buoyancy number from $B = 0.6$ to 5 (i.e., density differences from 1.8% to 15%) leads to an increase in the maximum pile height in our reference case from ∼150 km to more than 300 km (maximum pile volume from 5.5% to 30%). Similarly, additional convection controlling parameters affect the pile size. In particular, the additional internal heating as well as the depth-dependent expansion coefficient, which both reduce the effective Rayleigh number, again give vast piles which are stable for longer times. For example, the reference case with an additional internal heating of $H = 1$ (i.e., ∼80% internal heating) increases the pile volume from 9% to 20% and the maximum height from 230 to 830 km. Therefore convection parameters can possibly compensate for the low chemical influx at more realistic high Lewis numbers.

But also the chosen model geometry will play an important role. To minimize computation time we employed 2D Cartesian models for our parameter study. In this way we possibly exaggerate the pile size due to the unrealistically large bottom boundary. However, as our results show that infiltration occurs mostly beneath cold subducted slabs, the larger volume of the cold top boundary in spherical geometries might even increase the chemical influx. Linear downwellings have been reported in some spherical shell models when plate motion

is present, in particular the temperature-dependent viscosity seems to strengthen the cold linear downwellings (Zhong et al., 2000). Also, the work of Langemeyer et al. (2022) shows slabs buckling at the CMB, giving large areas in which the dense material is pushed aside. This seems to be even more pronounced for an increased contrast in composition-dependent viscosity. Likewise the consideration of low-viscosity post-perovskite leads to cold slabs vastly spreading above the CMB (Y. Li et al., 2014a; Nakagawa & Tackley, 2011). Future works will have to reveal how large these effects really are, but we do not expect an alteration of the general observation, that is, the penetration of dense core material into the mantle.

Closely related to the pile size is their survival time. Typically larger modeled piles exist longer, so that the piles in the primordial layer scenario are more persistent the greater the volume of the initial dense layer. In the core-mantle interaction scenario the piles exist even longer due to the constant basal influx that balances the entrainment.

As the survival time of piles also depends on entrainment, the life time of piles is strongly dependent on the convection. Olson and Kincaid (1991) and Tackley (2011) discuss that the stability of chemical structures depends on the ratio of entrainment (destabilizing thermal buoyancy) to enrichment (stabilizing compositional buoyancy). As mentioned above, a higher Rayleigh number promotes entrainment and thus reduces the survival time, but a higher Lewis number prevents entrainment. Using the tracer approach with the infinite Lewis number (i.e., a negligible chemical diffusion) shows that piles in the no flux cases also do not vanish during the life time of the Earth (Figure S5 in Supporting Information S1). The stability of piles has greatly been discussed (e.g., Jellinek & Manga, 2004; Mulyukova et al., 2015; Tan et al., 2011; Trim et al., 2020) and similar to our results it was found that dense dome-like structures survive for more than 3 Gyrs if assuming a high density contrast to prevent erosion by entrainment and mixing in the mantle (e.g., McNamara et al., 2010; Tan et al., 2011). Koelemeijer (2020), however, argues that the excess density to preserve structures in numerical models is typically larger than predicted by seismological observations. In our model setup the chemical influx allows for temporal stability also at low buoyancy ratios.

Besides the temporal stability additionally a spatial stability of the structures was discussed. For example, Tan et al. (2011) observed moving structures, which we also see in both our scenarios. However, it has been suggested from the reconstructions of eruption sites of LIPs and kimberlites that there is little movement of thermochemical structures in the last 300 Myr (e.g., Torsvik et al., 2006). We have already observed that piles are strongly coupled to the style of convection, so that a weak convective flow with almost stationary and wide plumes will also lead to broad, temporally and spatially chemical structures. In a future study it has to be investigated if and for how long our long-lived piles are stable in space. In particular a composition-dependent viscosity has been argued to stabilize piles spatially (e.g., Heyn et al., 2018). Our test cases with a mild composition-dependent viscosity did not confirm this result, maybe due to a too low composition-dependent viscosity contrast. In particular for the influx scenario with the smaller piles we did not observe a difference to the reference case, but a more thorough study on various fluid dynamical and rheological parameters with respect to pile stability is needed. For example, a more realistic pressure-dependent viscosity of $\Delta\eta_p = 30$ (e.g., Stein et al., 2004) could help to stabilize the piles more effectively as the increased viscosity not only acts within the piles but in the entire lower mantle.

Finally, assuming that a more realistic Lewis number would only give modeled pile heights of roughly 10 km, the additional internal heating and depth-dependent expansivity could play a role that leads to pile heights of up to 100 km. This is still very low when compared to LLSVPs but well in the assumed range of ULVZs (∼5–40 km high with a density increase of about 10%; Cottaar & Romanowicz, 2012; McNamara et al., 2010; Rost et al., 2006). In contrast, our primordial layer scenario gives larger structures and will thus more likely explain the large LLSVPs if a thick initial layer (∼10% of the mantle volume) is assumed. Therefore a combination of both scenarios seems most reasonable. The core material, that penetrates the mantle mainly beneath slabs, is pushed to the plumes where also the large piles reside, which form from the primordial dense layer. In this way the large LLSVPs and the smaller but denser ULVZs could maybe be established simultaneously. Possibly this also explains the proposed portion of core material in the mantle and the observed chemical signatures of OIBs as discussed in Torsvik et al. (2006). The mixing within the mantle needs to be analyzed in detail in future studies to find out if indeed enough entrained material reaches the surface to match the measurements at OIBs. Additionally the combination of scenarios using different chemical components will show if the simultaneous existence of ULVZs and LLSVPs can be obtained, or maybe subducted slabs will also have to be added (cf. Trønnes et al., 2019).

5. Summary

The observed ^{182}W deficits in ocean-island basalts (e.g., Rizo et al., 2019) show an excursion toward the core's tungsten isotopic composition (Kleine et al., 2009), so that an exchange between core and mantle material may occur (e.g., Hayden & Watson, 2007).

Applying a diffusive chemical influx at the base of thermochemical mantle convection models, we observe the self-consistent formation of a compositionally dense layer. Like in the scenario of a prescribed primordial dense layer, pile-like structures evolve from this layer. At the places where a cold downwelling slab sweeps dense accumulations aside and thins the thermochemical boundary layer, a higher chemical gradient is obtained than below the plume-pile complexes. Additionally, for strongly convecting systems we observe both that the dense material more quickly penetrates the mantle and that the piles erode faster due to entrainment of dense material to greater height. As penetration and entrainment is strongly controlled by the convective flow, the limiting effect of the very low chemical diffusivity (high Lewis number), can partly be overcome by the process of convection-assisted diffusion.

Nevertheless, the modeled piles forming in the influx scenario are generally smaller than for the primordial layer scenario. Therefore the primordial layer seems more suited to explain the large LLSVPs, while the smaller and denser ULVZs might be generated by iron-rich core material penetrating the mantle. The combination of the influx and primordial layer scenario can maybe explain the presence of various heterogeneities at the CMB as well as some core material in the mantle. In both scenarios we find that the dense material is swept to plumes, so maybe this can explain why ULVZs often reside at the edges of LLSVPs. Furthermore the infiltrated core material in our models is entrained by the convective upwellings, so that we also observe denser material at shallower depths.

Data Availability Statement

The code plaatjes used in this study predates open-source licensing and is not freely available. For replicability the numerical methods of the code are described in detail in Trompert and Hansen (1996), https://doi.org/10.1080/03091929608208968 and Tosi et al. (2015), https://doi.org/10.1002/2015GC005807. In the latter reference the code has also been benchmarked against several other (partly open-source) mantle convection codes. All data supporting the findings of this study are available in Stein and Hansen (2023): Replication Data for: Formation of Thermochemical Heterogeneities by Core-Mantle Interaction, https://doi.org/10.35003/JENO4T.

References

Ballmer, M. D., Lourenco, D. L., Hirose, K., Caracas, R., & Nomura, R. (2017). Reconciling magma-ocean crystallization models with the present-day structure of the Earth's mantle. *Geochemistry, Geophysics, Geosystems*, *7*, 2785–2806. https://doi.org/10.1002/2017gc006917

Bouffard, M., Choblet, G., Labrosse, S., & Wicht, J. (2019). Chemical convection and stratification in the Earth's outer core. *Frontiers of Earth Science*, *7*, 99. https://doi.org/10.3389/fearth.2019.00099

Brandenburg, J. P., & van Keken, P. E. (2007). Deep storage of oceanic crust in a vigorously convecting mantle. *Journal of Geophysical Research*, *112*(B6), B06403. https://doi.org/10.1029/2006JB004813

Brandon, A. D., & Walker, R. J. (2005). The debate over core-mantle interaction. *Earth and Planetary Science Letters*, *232*(3–4), 211–225. https://doi.org/10.1016/j.epsl.2005.01.034

Brandon, A. D., Walker, R. J., Morgan, J. W., Norman, M. D., & Pritchard, H. M. (1998). Coupled ^{186}Os and ^{187}Os evidence for core-mantle interaction. *Science*, *280*(5369), 1570–1573. https://doi.org/10.1126/science.280.5369.1570

Buffett, B. A., Garnero, E. J., & Jeanloz, R. (2000). Sediments at the top of Earth's core. *Science*, *290*(5495), 1338–1342. https://doi.org/10.1126/science.290.5495.1338

Bull, A. L., McNamara, A. K., & Ritsema, J. (2009). Synthetic tomography of plume clusters and thermochemical piles, Earth Planet. *Science Letter*, *278*(3–4), 152–162. https://doi.org/10.1016/j.epsl.2008.11.018

Cottaar, S., & Lekic, V. (2016). Morphology of seismically slow lower-mantle structures. *Geophysical Supplements to the Monthly Notices of the Royal Astronomical Society*, *207*(2), 1122–1136. https://doi.org/10.1093/gji/ggw324

Cottaar, S., & Romanowicz, B. (2012). An unusually large ULVZ at the base of the mantle near Hawaii. *Earth and Planetary Science Letters*, *355*, 213–222. https://doi.org/10.1016/j.epsl.2012.09.005

Davaille, A. (1999). Simultaneous generation of hotspots and superswells by convection in a heterogenous planetary mantle. *Nature*, *402*(6763), 756–760. https://doi.org/10.1038/45461

Dehant, V., Campuzano, S. A., De Santis, A., & van Westrenen, W. (2022). Structure, materials and processes in the Earth's core and mantle. *Surveys in Geophysics*, *43*, 1–40. https://doi.org/10.1007/s10712-021-09684-y

Deschamps, F., Cobden, L., & Tackley, P. J. (2012). The primitive nature of large low shear-wave velocity provinces. *Earth and Planetary Science Letters*, *349*, 198–208. https://doi.org/10.1016/j.epsl.2012.07.012

Deschamps, F., & Tackley, P. J. (2008). Searching for models of thermo-chemical convection that explain probabilistic tomography: I. Principles and influence of rheological parameters. *Physics of the Earth and Planetary Interiors*, *171*(1–4), 357–373. https://doi.org/10.1016/j.pepi.2008.04.016

Dziewonski, A. M. (1984). Mapping the lower mantle—Determination of lateral heterogeneity in P-velocity up to degree and order 6. *Journal of Geophysical Research*, *89*(B7), 5929–5952. https://doi.org/10.1029/jb089ib07p05929

Forte, A. M., & Mitrovica, J. X. (2001). Deep-mantle high viscosity flow and thermochemical structure inferred from seismic and geodynamic data. *Nature*, *410*(6832), 1049–1056. https://doi.org/10.1038/35074000

Frost, D. A., & Rost, S. (2014). The P-wave boundary of the large-low shear velocity province beneath the Pacific. *Earth and Planetary Science Letters*, *403*, 380–392. https://doi.org/10.1016/j.epsl.2014.06.046

Garnero, E. J. (2000). Heterogeneity of the lowermost mantle. *Annual Review of Earth and Planetary Sciences*, *28*(1), 509–537. https://doi.org/10.1146/annurev.earth.28.1.509

Garnero, E. J., & McNamara, A. K. (2008). Structure and dynamics of Earth's lower mantle. *Science*, *320*(5876), 626–628. https://doi.org/10.1126/science.1148028

Garnero, E. J., McNamara, A. K., & Shim, S.-H. (2016). Continent-sized anomalous zones with low seismic velocity at the base of Earth's mantle. *Nature Geoscience*, *9*(7), 481–489. https://doi.org/10.1038/ngeo2733

Garnero, E. J., Revenaugh, J. S., Williams, Q., Lay, T., & Kellogg, L. H. (1989). Ultralow velocity zone at the core–mantle boundary. In *The core–mantle boundary region* (pp. 319–334).

Gleeson, M., Soderman, C., Matthews, S., Cottaar, S., & Gibson, S. (2021). Geochemical constraints on the structure of the Earth's deep mantle and the origin of the LLSVPs. *Geochemistry, Geophysics, Geosystems*, *22*(9), e2021GC009932. https://doi.org/10.1029/2021GC009932

Grand, S. P., van der Hilst, R. D., & Widiyantoro, S. (1997). Global seismic tomography: A snapshot of convection in the Earth. *Geological Society of America Today*, *7*, 1–7.

Gurnis, M. (1986). The effects of chemical density differences on convective mixing in the Earth's mantle. *Journal of Geophysical Research*, *91*(B11), 11407–11419. https://doi.org/10.1029/jb091ib11p11407

Hansen, U., & Yuen, D. A. (1988). Numerical simulations of thermal-chemical instabilities at the core-mantle boundary. *Nature*, *334*(6179), 237–240. https://doi.org/10.1038/334237a0

Hayden, L. A., & Watson, E. B. (2007). A diffusion mechanism for core-mantle interaction. *Nature*, *250*(7170), 709–712. https://doi.org/10.1038/nature06380

Hernlund, J. W., & Houser, C. (2008). On the statistical distribution of seismic velocities in Earth's deep mantle. *Earth and Planetary Science Letters*, *265*(3–4), 423–437. https://doi.org/10.1016/j.epsl.2007.10.042

Heyn, B. H., Conrad, C. P., & Trønnes, R. G. (2018). Stabilizing effect of compositional viscosity contrasts on thermochemical piles. *Geophysical Research Letters*, *45*(15), 7523–7532. https://doi.org/10.1029/2018gl078799

Huang, J., & Davies, G. F. (2006). Stirring in three-dimensional mantle convection models and implications for geochemistry: 2. Heavy tracers. *Geochemistry, Geophysics, Geosystems*, *8*(7), Q07004. https://doi.org/10.1029/2007GC001621

Ishii, M., & Tromp, J. (1999). Normal-mode and free-air gravity constraints on lateral variations in velocity and density of Earth's mantle. *Science*, *285*(5431), 1231–1236. https://doi.org/10.1126/science.285.5431.1231

Jellinek, A. M., & Manga, M. (2004). Links between long-lived hot spots, mantle plumes, D″, and plate tectonics. *Reviews of Geophysics*, *42*(3), 2003RG000144. https://doi.org/10.1029/2003rg000144

Jones, T. D., Maguire, R. R., Keken, P. E., Ritsema, J., & Paula Koelemeijer, P. (2020). Subducted oceanic crust as the origin of seismically slow lower-mantle structures. *Progress in Earth and Planetary Science*, *7*, 1–16. https://doi.org/10.1186/s40645-020-00327-1

Kanda, R. V. S., & Stevenson, D. J. (2006). Suction mechanism for iron entrainment into the lower mantle. *Geophysical Research Letters*, *33*(2), L02310. https://doi.org/10.1029/2005gl025009

Kellogg, L. H., Hager, B. H., & van der Hilst, R. D. (1999). Compositional stratification in the deep mantle. *Science*, *283*(5409), 1881–1884. https://doi.org/10.1126/science.283.5409.1881

Kellogg, L. H., & Turcotte, D. (1987). Homogenization of the mantle by convective mixing and diffusion. *Earth and Planetary Science Letters*, *81*(4), 371–378. https://doi.org/10.1016/0012-821x(87)90124-5

Kleine, T., Touboul, M., Bourdin, B., Nimmo, F., Mezger, J., Palme, H., et al. (2009). Hf-W chronology of the accretion and early evolution of asteroids and terrestrial planets. *Geochimica et Cosmochimica Acta*, *73*(17), 5150–5188. https://doi.org/10.1016/j.gca.2008.11.047

Knittle, E., & Jeanloz, R. (1991). Earth's core-mantle boundary: Results of experiments at high pressures and temperatures. *Science*, *251*(5000), 1438–1443. https://doi.org/10.1126/science.251.5000.1438

Koelemeijer, P. (2020). Towards consistent seismological models of the core-mantle boundary landscape. *Earth and Space Science Open Archive*. https://doi.org/10.1002/essoar.10502426.1

Kuwayama, Y., Hirose, K., Cobden, L., Kusakabe, M., Tateno, S., & Ohishi, Y. (2022). Post-perovskite phase transition in the pyrolitic lowermost mantle: Implications for ubiquitous occurrence of post-perovskite above CMB. *Geophysical Research Letters*, *49*(1), e2021GL096219. https://doi.org/10.1029/2021GL096219

Labrosse, S., Hernlund, J. W., & Coltice, N. (2007). A crystallizing dense magma ocean at the base of the Earth's mantle. *Nature*, *450*(7171), 866–869. https://doi.org/10.1038/nature06355

Laneuville, M., Hernlund, J., Labrosse, S., & Guttenberg, N. (2018). Crystallization of a compositionally stratified basal magma ocean. *Physics of the Earth and Planetary Interiors*, *276*, 86–92. https://doi.org/10.1016/j.pepi.2017.07.007

Langemeyer, S. M., Lowman, J. P., & Tackley, P. J. (2020). The dynamics and impact of compositionally originating provinces in a mantle convection model featuring rheologically obtained plates. *Geophysical Journal International*, *220*(3), 1700–1716. https://doi.org/10.1093/gji/ggz497

Langemeyer, S. M., Lowman, J. P., & Tackley, P. J. (2022). Contrasts in two- and three-dimensional system behaviour in the modelling of compositionally originating LLSVPs and a mantle featuring dynamically obtained plates. *Geophysical Journal International*, *230*(3), 1751–1774. https://doi.org/10.1093/gji/ggac143

Lassak, T. M., McNamara, A. K., Garnero, E., & Zhong, S. (2010). Core-mantle boundary topography as a possible constraint on lower mantle chemistry and dynamics. *Earth and Planetary Science Letters*, *289*(1–2), 232–241. https://doi.org/10.1016/j.epsl.2009.11.012

Lassak, T. M., McNamara, A. K., & Zhong, S. (2007). Influence of thermochemical piles on topography at Earth's core-mantle boundary. *Earth and Planetary Science Letters*, *261*(3–4), 443–455. https://doi.org/10.1016/j.epsl.2007.07.015

Lay, T. (2015). Deep Earth structure—Lower mantle and D. In *Treatise on geophysics 1: Seismology and the structure of the Earth* (pp. 683–723).

Lay, T., Williams, Q., & Garnero, E. J. (1998). The core-mantle boundary layer and deep Earth dynamics. *Nature*, *392*(6675), 461–468. https://doi.org/10.1038/33083

Lee, C., Luffi, P., Höink, T., Li, J., Dasgupta, R., & Hernlund, J. (2010). Upside-down differentiation and generation of a 'primordial' lower mantle. *Nature*, *463*(7283), 930–933. https://doi.org/10.1038/nature08824

Li, M., & McNamara, A. (2013). The difficulty for subducted oceanic crust to accumulate at the Earth's core-mantle boundary. *Journal of Geophysical Research: Solid Earth*, *118*(4), 1807–1816. https://doi.org/10.1002/jgrb.50156

Li, M., McNamara, A. K., & Garnero, E. J. (2014). Chemical complexity of hotspots caused by cycling oceanic crust through mantle reservoirs. *Nature Geoscience*, *7*(5), 336–370. https://doi.org/10.1038/ngeo2120

Li, Y., Deschamps, F., & Tackley, P. J. (2014a). Effects of low-viscosity post-perovskite on the stability and structure of primordial reservoirs in the lower mantle. *Geophysical Research Letters*, *41*(20), 7089–7097. https://doi.org/10.1002/2014GL061362

Li, Y., Deschamps, F., & Tackley, P. J. (2014b). The stability and structure of primordial reservoirs in the lower mantle: Insights from models of thermochemical convection in three-dimensional spherical geometry. *Geophysical Journal International*, *199*(2), 914–930. https://doi.org/10.1093/gji/ggu295

Li, Y., Deschamps, F., Yang, J., Chen, L., Zhao, L., & Tackley, P. J. (2019). Effects of the compositional viscosity ratio on the long-term evolution of thermochemical reservoirs in the deep mantle. *Geophysical Research Letters*, *46*(16), 9591–9601. https://doi.org/10.1029/2019GL083668

Mao, W. L., Mao, H. K., Sturhahn, W., Zhao, J., Prakapenka, V. B., Meng, Y., et al. (2006). Iron-rich post-perovskite and the origin of ultralow-velocity zones. *Science*, *312*(5773), 564–565. https://doi.org/10.1126/science.1123442

McNamara, A. K. (2019). A review of large low shear velocity provinces and ultra low velocity zones. In *Linking plate tectonics and volcanism to deep Earth dynamics—A tribute to Trond H. Torsvik, tectonophysics* (Vol. 760, pp. 199–220).

McNamara, A. K., Garnero, E., & Rost, S. (2010). Tracking deep mantle reservoirs with ultra-low velocity zones. *Earth and Planetary Science Letters*, *229*(1–2), 1–9. https://doi.org/10.1016/j.epsl.2010.07.042

McNamara, A. K., & Zhong, S. (2005). Thermochemical structures beneath Africa and the Pacific Ocean. *Nature*, *437*(7062), 1136–1139. https://doi.org/10.1038/nature04066

Meyer, A., Hennig, L., Kargl, F., & Unruh, T. (2019). Iron self diffusion in liquid pure iron and iron-carbon alloys. *Journal of Physics: Condensed Matter*, *31*(39), 395401. https://doi.org/10.1088/1361-648X/ab2855

Mulyukova, E., Steinberger, B., Dabrowski, M., & Sobolev, S. V. (2015). Survival of LLSVPs for billions of years in a vigorously convecting mantle: Replenishment and destruction of chemical anomaly. *Journal of Geophysical Research: Solid Earth*, *120*(5), 3824–3847. https://doi.org/10.1002/2014jb011688

Mundl, A., Touboul, M., Jackson, M. G., Day, J. M. D., Kurz, M. D., Lekic, V., et al. (2017). Tungsten-182 heterogeneity in modern ocean island basalts. *Science*, *356*(6333), 66–69. https://doi.org/10.1126/science.aal4179

Murakami, N., Hirose, K., Kawamura, K., Sata, N., & Ohishi, Y. (2004). Post-perovskite phase transition in. *MgSiO3 Science*, *304*(5672), 855–858. https://doi.org/10.1126/science.1095932

Nakagawa, T., & Tackley, P. J. (2011). Effects of low-viscosity post-perovskite on thermo-chemical mantle convection in a 3-D spherical shell. *Geophysical Research Letters*, *38*(4), L04309. https://doi.org/10.1029/2010GL046494

Ni, S., & Helmberger, D. (2003). Further constraints on the African superplume structure. *Physics of the Earth and Planetary Interiors*, *140*(1–3), 243–251. https://doi.org/10.1016/j.pepi.2003.07.011

Niu, Y. (2018). Origin of the LLSVPs at the base of the mantle is a consequence of plate tectonics—A petrological and geochemical perspective. *Geoscience Frontiers*, *9*(5), 1265–1278. https://doi.org/10.1016/j.gsf.2018.03.005

O'Farrell, K. A., & Lowman, J. P. (2010). Emulating the thermal structure of spherical shell convection in plane-layer geometry mantle convection models. *Physics of the Earth and Planetary Interiors*, *182*(1–2), 73–84. https://doi.org/10.1016/j.pepi.2010.06.010

Oganov, A. R., & Ono, S. (2004). Theoretical and experimental evidence for a post-perovskite phase of MgSiO₃ in Earth's D″ layer. *Nature*, *430*(6998), 445–448. https://doi.org/10.1038/nature02701

Olson, P., & Kincaid, C. (1991). Experiments on the interaction of thermal convection and compositional layering at the base of the mantle. *Journal of Geophysical Research*, *96*(B3), 4347–4354. https://doi.org/10.1029/90jb02530

Otsuka, K., & Karato, S. I. (2012). Deep penetration of molten iron into the mantle caused by a morphological instability. *Nature*, *492*(7428), 243–247. https://doi.org/10.1038/nature11663

Petford, N., Yuen, D., Rushmer, T., Brodholt, J., & Stackhouse, S. (2005). Shear-induced material transfer across the core-mantle boundary aided by the post-perovskite phase transition. *Earth Planets and Space*, *57*(5), 459–464. https://doi.org/10.1186/bf03351834

Poirier, J.-P., & Le Mouël, J.-L. (1992). Does infiltration of core material into the lower mantle affect the observed geomagnetic field? *Physics of the Earth and Planetary Interiors*, *73*(1–2), 29–37. https://doi.org/10.1016/0031-9201(92)90105-5

Rizo, H., Andrault, D., Bennett, N. R., Humayun, M., Brandon, A., Vlastelic, I., et al. (2019). ¹⁸²W evidence for core-mantle interaction in the source of mantle plumes. *Geochemical Perspectives Letters*, *11*, 6–11. https://doi.org/10.7185/geochemlet.1917

Romanowicz, B. (2001). Can we resolve 3D density heterogeneity in the lower mantle? *Geophysical Research Letters*, *28*(6), 1107–1110. https://doi.org/10.1029/2000gl012278

Rost, S., Garnero, E. J., & Williams, Q. (2006). Fine-scale ultralow-velocity zone structure from high-frequency seismic array data. *Journal of Geophysical Research*, *111*(B9), B09310. https://doi.org/10.1029/2005JB004088

Rost, S., Garnero, E. J., Williams, Q., & Manga, M. (2005). Seismological constraints on a possible plume root at the core–mantle boundary. *Nature*, *435*(7042), 666–669. https://doi.org/10.1038/nature03620

Schubert, G., Masters, G., Olson, P., & Tackley, P. J. (2004). Superplumes or plume clusters? *Physics of the Earth and Planetary Interiors*, *146*(1–2), 147–162. https://doi.org/10.1016/j.pepi.2003.09.025

Solomatov, V. S. (2015). Magma Oceans and primordial mantle differentiation. In *Evolution of the Earth*. In *Treatise on geophysics* (Vol. 9, pp. 81–104).

Stein, C., & Hansen, U. (2023). Replication data for: Formation of thermochemical heterogeneities by core-mantle interaction. TRR170-DB, V1. https://doi.org/10.35003/JENO4T

Stein, C., Lowman, J. P., & Hansen, U. (2013). The influence of mantle internal heating on lithospheric mobility: Implications for super-Earths. *Earth and Planetary Science Letters*, *361*, 448–459. https://doi.org/10.1016/j.epsl.2012.11.011

Stein, C., Mertens, M., & Hansen, U. (2020). A numerical study of thermal and chemical structures at the core-mantle boundary. *Earth and Planetary Science Letters*, *548*, 116498. https://doi.org/10.1016/j.epsl.2020.116498

Stein, C., Schmalzl, J., & Hansen, U. (2004). The effect of rheological parameters on plate behaviour in a self-consistent model of mantle convection. *Earth and Planetary Science Letters*, *142*(3–4), 225–255. https://doi.org/10.1016/j.pepi.2004.01.006

Steinberger, B., & Torsvik, T. H. (2012). A geodynamic model of plumes from the margins of large low shear velocity provinces. *Geochemistry, Geophysics, Geosystems*, *13*(1), Q01W09. https://doi.org/10.1029/2011GC03808

Sun, D., Helmberger, D., Ni, S., & Bower, D. (2009). Direct measures of lateral velocity variation in the deep Earth. *Journal of Geophysical Research*, *114*, B05303. https://doi.org/10.1029/2008jb005873

Tackley, P. J. (2011). Living dead slabs in 3-D: The dynamics of compositionally-stratified slabs entering a 'slab graveyard' above the core-mantle boundary. *Physics of the Earth and Planetary Interiors*, *188*(3–4), 150–162. https://doi.org/10.1016/j.pepi.2011.04.013

Tan, E., & Gurnis, M. (2007). Compressible thermo-chemical convection and application to lower mantle superplumes. *Journal of Geophysical Research*, *112*(B6), B06304. https://doi.org/10.1029/2006JB004505

Tan, E., Leng, W., Zhong, S., & Gurnis, M. (2011). On the location of plumes and lateral movement of thermochemical structures with high bulk modulus in the 3-D compressible mantle. *Geochemistry, Geophysics, Geosystems*, *12*(7), Q07005. https://doi.org/10.1029/2011GC003665

Torsvik, T., Smethurst, M., Burke, K., & Steinberger, B. (2006). Large igneous provinces generated from the margins of the large low-velocity provinces in the deep mantle. *Geophysical Journal International*, *167*(3), 1447–1460. https://doi.org/10.1111/j.1365-246x.2006.03158.x

Tosi, N., Stein, C., Noack, L., Hüttig, C., Maierova, P., Samuel, H., et al. (2015). A community benchmark for viscoplastic thermal convection in a 2-D square box. *Geochemistry, Geophysics, Geosystems*, *16*(7), 2175–2196. https://doi.org/10.1002/2015gc005807

Trim, S. J., Heron, P., Stein, C., & Lowman, J. P. (2014). The feedback between surface mobility and mantle compositional heterogeneity: Implications for the Earth and other terrestrial planets. *Earth and Planetary Science Letters*, *405*(1–14), 782–814. https://doi.org/10.1016/j.epsl.2014.08.019

Trim, S. J., & Lowman, J. P. (2016). Interaction between the supercontinent cycle and the evolution of intrinsically dense provinces in the deep mantle. *Journal of Geophysical Research: Solid Earth*, *121*(12), 8941–8969. https://doi.org/10.1002/2016JB013285

Trim, S. J., Lowman, J. P., & Butler, S. L. (2020). Improving mass conservation with the tracer ratio method: Application to thermochemical mantle flows. *Geochemistry, Geophysics, Geosystems*, *22*(2), e2019GC008799. https://doi.org/10.1029/2019GC008799

Trompert, R. A., & Hansen, U. (1996). The application of a finite volume multigrid method to three-dimensional flow problems in a highly viscous fluid with a variable viscosity. *Geophysical & Astrophysical Fluid Dynamics*, *83*, 261–291. https://doi.org/10.1080/03091929608208968

Trønnes, R. G., Baron, M. A., Eigenmann, K. R., Guren, M. G., Heyn, B. H., Løken, A., & Mohn, C. E. (2019). Core formation, mantle differentiation and core-mantle interaction within Earth and the terrestrial planets. *Tectonophysics*, *760*, 165–198. https://doi.org/10.1016/j.tecto.2018.10.021

Walker, R. J., & Walker, D. (2005). Does the core leak? *Eos, Transactions American Geophysical Union*, *86*(25), 237–244. https://doi.org/10.1029/2005eo250001

Wen, L. (2001). Seismic evidence for a rapidly-varying compositional anomaly at the base of the Earth's mantle beneath Indian Ocean. *Earth and Planetary Science Letters*, *194*(1–2), 83–95. https://doi.org/10.1016/s0012-821x(01)00550-7

Wicks, J. K., Jackson, J. M., & Sturhahn, W. (2010). Very low sound velocities in iron- rich (Mg, Fe)O: Implications for the core-mantle boundary region. *Geophysical Research Letters*, *37*(15), L15304. https://doi.org/10.1029/2010gl043689

Zaranek, S. E., & Parmentier, E. M. (2004). Convective cooling of an initially stably stratified fluid with temperature-dependent viscosity: Implications for the role of solid-state convection in planetary evolution. *Journal of Geophysical Research*, *109*(B3), B03409. https://doi.org/10.1029/2003JB002462

Zhong, S., & Gurnis, M. (1997). Dynamic interaction between tectonic plates, subducting slabs, and the mantle, *Earth Interactions*. *1*, 1–18, https://doi.org/10.1175/1087-3562(1997)001<0001:DIBTPS>2.3.CO;2

Zhong, S., Zuber, M. T., Moresi, L., & Gurnis, M. (2000). Role of temperature-dependent viscosity and surface plates in spherical shell models of mantle convection. *Journal of Geophysical Research*, *105*(B5), 11063–11082. https://doi.org/10.1029/2000JB900003